Thesis for the degree of Licentiate of Philosophy

An ALMA perspective on massive high-redshift galaxy evolution

Kiana Kade

CHALMERS
UNIVERSITY OF TECHNOLOGY

Department of Space, Earth and Environment
Division of Astronomy and Plasma Physics
Chalmers University of Technology
Gothenburg, Sweden 2022

An ALMA perspective on massive high-redshift galaxy evolution

Kiana Kade

Division of Astronomy and Plasma Physics
Department of Space, Earth and Environment
Chalmers University of Technology
SE-412 96 Gothenburg
Telephone +46 31 772 1000

Contact information:
Kiana Kade
Onsala Space Observatory
Chalmers University of Technology
SE–439 92 Onsala, Sweden

Phone: +46 (0)31 772 55 44
Email: kiana.kade@chalmers.se

Cover image: *Artist conception of the galaxy W2246-0526*
Credit: NRAO/AUI/NSF/S. Dagnello.

Printed by Chalmers Reproservice
Gothenburg, Sweden 2022

An ALMA perspective on massive high-redshift galaxy evolution

Kiana Kade
Department of Space, Earth and Environment
Chalmers University of Technology

Abstract

The processes governing the growth and evolution of high-redshift massive galaxies have long been a subject of intense investigations. Studies of the cosmic star-formation rate density have shown a peak at $z \sim 2-3$, demonstrating the distinct need to understand the mechanisms by which galaxies acquired the fuel necessary to ignite such intense star-formation. Galaxies are expected to transform through a number of phases leading up to and proceeding this peak. Theoretical modelling and simulations have proposed several driving mechanisms to cause these changes, including feedback from active galactic nuclei and merger activity driven by the effect of companion galaxies. However, both of these can be difficult to observe at high-redshift and studies have concluded conflicting results in the past decades. A synergy must exist between the predictions of theoretical simulations and observational realities; with the increased sensitivity and capability of modern telescopes it has become possible to investigate this.

Observations probing the effect of these mechanisms in the high-redshift universe have greatly improved in recent years with the advent of telescopes such as the Atacama Large submillimeter/Millimeter Array. Through observations of the environment of massive high-redshift quasars and starburst galaxies, along with detections of companion galaxies, it has become possible to begin to understand the effect these companions could have. Furthermore, signatures of outflow activity and tracers of the impact of active galactic nuclei on their host galaxy have begun to uncover the significance of feedback in high-redshift galaxies.

This licentiate thesis summarizes the current understanding of massive high-redshift galaxy evolution and presents two (possibly archetypal) examples of massive high-redshift galaxies. Using deep, high-resolution observations of the far-infrared fine structure [C II] 158 μm line, faint companions were found in close proximity to both the quasar BRI0952-0115 ($z = 4.432$) and the sumbillimeter galaxy AzTEC-3 ($z = 5.3$). Additionally, both BRI0952 and AzTEC-3 exhibit signatures of outflows. The results presented in Paper I provide additional evidence to the hypothesis that massive high-redshift galaxies evolve in over-dense regions and that outflow activity can have a dramatic effect on the host galaxy. Moreover, they demonstrate the necessity of conducting deeper observations necessary to detect these relatively fainter phenomena that are thought to be a crucial aspect of galaxy evolution.

Keywords: Galaxies: evolution – Galaxies: high-redshift – Galaxies: AGN – Galaxies: starbursts – techniques: interferometric

Research Contributions

This thesis is based on the work contained in the following papers:

I **Kade K.**, Knudsen K. K., Vlemmings W., Stanley F., Gullberg B., König S.: *Exploring the environment, magnetic fields, and feedback effects of massive high-redshift galaxies with* [C II]
Submitted to Astronomy & Astrophysics

Acknowledgements

First and foremost a huge thank you to my supervisor, Kirsten, for being constantly available, flexible, compassionate, and always up for answering whatever questions I might have. She also provided me with support throughout the Covid-19 pandemic, but specifically in the beginning when I was very new to Gothenburg. I would also like to thank the ever changing members of my research group: Flora, Bitten, Jan, JB, and Madeleine for their help in making me feel welcome, writing my first paper, and writing this licentiate thesis. Thank you my close friend Holly for existing, understanding all my weird references, of course for reading and editing this licentiate. Thank you to Mark & Amy, Andri, and the rest of the division for their help, support, and friendship. Thank you to my family for supporting my love my science and my desire to study galaxies. Finally, thank you to my partner Ariel for reading my favorite books (even when they're 'super-nerdy') and always supporting me.

As the Earth shrinks, the universe stretches forth its beckoning hand in a gesture to all mankind
- Public Service Broadcasting

CONTENTS

CHAPTER 1

INTRODUCTION

1.1 A brief history of the universe

The origin of the universe can be described as a 'Big Bang' followed by a period of intense inflation during which the universe expanded rapidly. The driving mechanisms of this rapid expansion are currently an open question in cosmology. The high temperatures and densities following the Big Bang resulted in the constitute matter of the universe being merely a sea of plasma: that is, a sea of protons and electrons swarming across the universe. As the universe continued to expand, temperatures and densities decreased sufficiently for the recombination of this plasma into protons and electrons. The radiation released by the process of recombination has been termed the 'Cosmic Microwave Background' (CMB) and is the most distant radiation observed in the universe.

Following the conclusion of recombination there was no significant source of radiation in the universe. Thus, the universe entered the 'cosmic dark ages'. During this time no light was emitted and the universe was composed entirely of neutral hydrogen and helium. Inhomogeneities in dark matter distribution grew and baryonic matter in the most massive eventually coalesced through gravitational collapse. This led to the formation of more familiar structures such as stars and eventually galaxies.

The appearance of the first stars and galaxies marks the beginning of the period commonly referred to as 'reionization'. Prior to the formation of the first stars (termed Pop. III stars), the hydrogen and helium in the universe was in its neutral state. These early stars, and subsequent galaxies, began re-ionizing the hydrogen in the universe with ultraviolet (UV) photons. Stars effectively created 'bubbles' of re-ionized hydrogen around them. These bubbles expanded around their stars until an entire galaxy was functionally an ionizing bubble. This process began at $z \sim 20$ (Planck Collaboration et al. 2016) and continued until a redshift [1](z) of

[1]Redshift is an astronomical term relating to the phenomenon of light from distant objects shifting to redder wavelengths due to the expansion of the universe. It is a ratio that can be calculated according to $z = \frac{\lambda_{\text{obs}} - \lambda_{\text{emit}}}{\lambda_{\text{emit}}}$, where λ_{emit} is the rest-frame wavelength of the light and λ_{obs} is the observed wavelength.

$z \sim 6$ corresponding to about one billion years after the Big Bang, as indicated by a number of probes thought to trace ionization levels, such as Lyman-α emission and Gamma-ray bursts (e.g., Stark 2016).

The completion of the process of reionization marks the last large-scale property change of baryonic matter in the universe. The process by which massive galaxy evolution proceeded from this period is an open question and the main topic of the this licentiate thesis.

1.2 Galaxies across cosmic time

An imperative aspect of understanding how galaxies look in the local universe (i.e., those located relatively 'nearby' the Milky Way) is to determine the evolutionary processes that led to their morphology and characteristics. Naturally, this requires the study of the predecessors of the Milky Way and thus the study of the high-redshift universe. Observations of distances very far from Earth effectively look backwards in time, allowing for the characterization of the properties observed with increasing redshift, and the study how different galaxies grew and transformed.

Galaxies look different with increasing redshift suggesting that the evolutionary processes governing high-redshift galaxies were very different than those affecting the local universe and the Milky Way (e.g., Papovich et al. 2005). Increasing redshift leads to a general decrease in structure of the galaxies, an increase in the star-formation rate density, and a decrease in galaxy mass for massive galaxies (e.g., Conselice 2014; Madau & Dickinson 2014).

Galaxies are known to grow in conjunction with their dark matter halos (e.g., Kormendy & Ho 2013) primarily through accretion and mergers. The environment in which a galaxy evolves has a measurable impact on its development and growth. The most massive galaxies tend to form in more crowded environments (e.g., Springel et al. 2005; Vogelsberger et al. 2014), which in turn form along filamentary structures of dark matter distribution. Alternatively, some galaxies may develop in 'voids' or the less-dense spaces between dark matter filaments (Kreckel et al. 2011), but these galaxies appear to be relatively rare.

The general understanding of galaxy evolution is a constantly evolving landscape. The breadth of galaxy characteristics, such as mass, dust content, star-formation rate, and environment lead to a wide range of possibilities when attempting to derive a common evolutionary path through the extensive variety of observed galaxies. The puzzle of galaxy evolution is, as of yet, unsolved.

1.3 Summary of this thesis

Investigating the early universe and the ways in which galaxies evolved at high-redshift is paramount to understanding how our Milky Way formed and the place our home has in the fascinating tale of galaxy evolution. It is only by studying the presumed progenitors of galaxies today, that is to say massive galaxies in the early universe, that it is possible to come to an understanding of how this evolution progressed.

This licentiate thesis aims to discuss the ways in which massive galaxies, specifically between $4 < z < 6$, evolve and the different factors that affect this evolution. The work presented focuses on the role of the environment and the effect of the central supermassive black hole (SMBH) on its host galaxy. The incredible increase in technological capacity afforded in recent years has led to a dramatic escalation in direct observations of the environment of high-redshift galaxies. However, the results of these observations still have unclear ramifications as to the overall effect the environments in which these massive galaxies evolve have on them. Additionally, probes of the effect of active galactic nuclei (AGN) in the high-redshift universe have expanded ten-fold in recent years, although there remains too large a gap between theoretical models and the results of observational studies to establish conclusive scenarios.

The work presented in this thesis provides the background for, and results of, a case-study of two galaxies during this epoch. By comparing these galaxies to each other, and to other observational evidence, it is possible to contrast empirical findings thus far with currently accepted scenarios of massive galaxy evolution. Through investigating the environment of both, along with their individual properties determined through radio observations, these galaxies appear to exhibit the sought-after characteristics that may begin to untangle some of the mysteries of high-redshift galaxy evolution.

CHAPTER 2

GALAXY FORMATION & EVOLUTION

In the nearby universe galaxies are often classified into two distinct categories: early and late types. Early-type galaxies, such as elliptical galaxies, are typically more massive with very low rates of star formation and older stellar populations (e.g., Schawinski et al. 2014). Late-type galaxies, such as spiral galaxies, are typically less massive, more gas rich, and have higher rates of star formation (e.g., Schawinski et al. 2014). This is shown in Figure 2.1. A first step to determining the evolution of these populations is by investigating different mechanisms of galaxy growth.

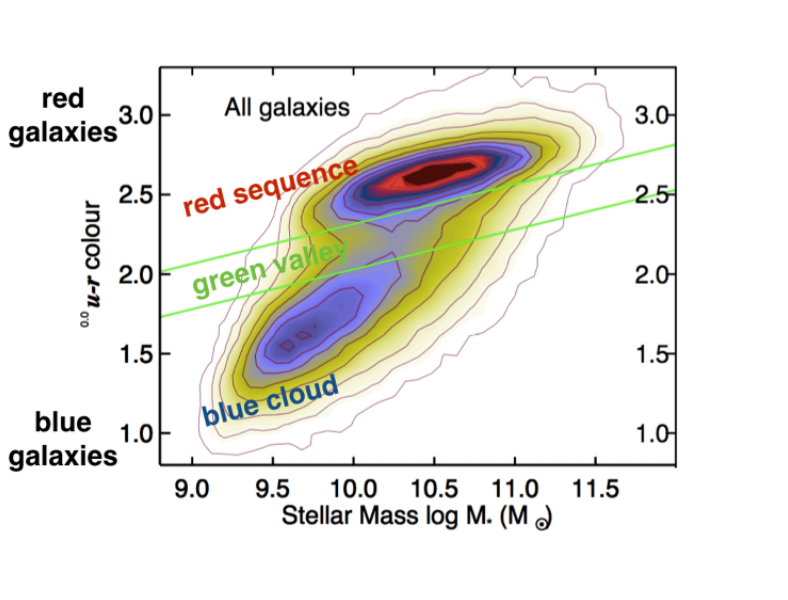

Figure 2.1: The galaxy color diagram showing the color of a galaxy (u-r filter flux) as a function of the stellar mass of a given galaxy. It is clear that the red sequence (elliptical/early-type galaxies) are, on average, significantly more massive than the blue cloud (spiral/late-type galaxies). Figure from Schawinski et al. (2014).

Studying the rate of star formation as a function of cosmic time is crucial to a robust understanding of galaxy evolution. A variety of star-formation probes

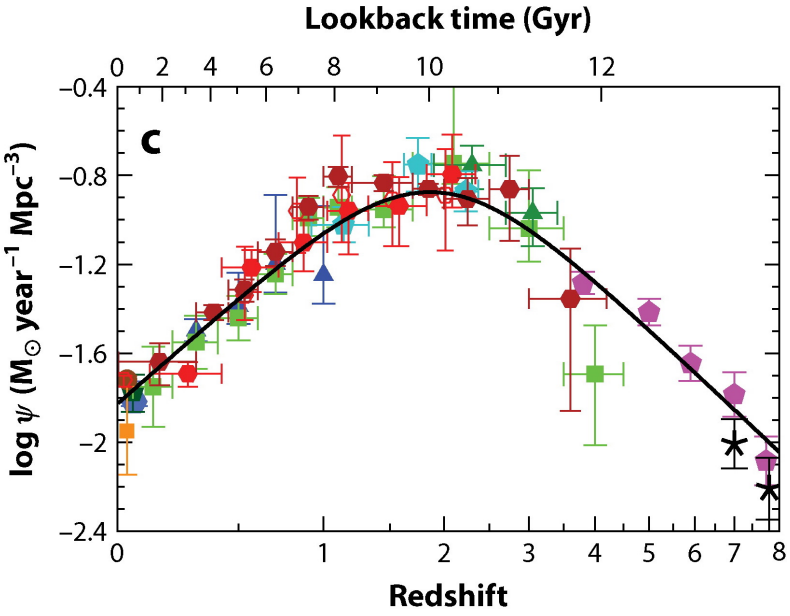

Figure 2.2: The star-formation rate density as a function of redshift (bottom) or cosmic time (top). This clearly demonstrates the peak in cosmic-star formation at $z \sim 2-3$. Figure from Madau & Dickinson (2014).

are available across a wide range of frequencies; this allows for a more global determination of star formation rate (SFR) spanning a wide redshift range (see Madau & Dickinson (2014) for a review). The star formation rate as a function of redshift has been well studied and appears to peak at a redshift of $z \sim 2-3$, a period which has come to be termed 'cosmic noon'. The rate of star formation rose preceding to this redshift (i.e., $z > 2-3$) and fell proceeding (i.e., $z < 2-3$), shown in Figure 2.2. The rather obvious connection between a galaxy's rate of star formation and its gas content leads to the quandary of the origin of the increase to cosmic noon. How did galaxies in the early universe amass such fuel reserves to produce the extreme SFRs observed at cosmic noon? To answer this question it is necessary to understand how galaxies (both during this epoch and throughout cosmic time) grow and acquire gas and dust.

2.1 Main modes of galaxy growth

2.1.1 Gas accretion

One mechanism of galaxy growth is accretion. Through this process a galaxy accretes matter from the intergalactic medium (IGM) along dark matter filaments. As matter congeals along dark matter filaments gravity becomes an ever-increasingly dominant mechanism and the largest structures clump together. Galaxies themselves also typically form along these filaments with the most massive occurring at the intersections of different filamentary structures (e.g., Springel et al. 2005; Vogelsberger et al. 2014).

There exist two main modes of gas accretion: hot and cold mode accretion

(e.g., Katz et al. 2003; Kereš et al. 2005; Dekel et al. 2009; Di Matteo et al. 2012). Cold mode accretion funnels cold, $T_{\rm gas} \leq 10^5\,{\rm K}$, gas (i.e., gas with $T_{\rm gas} < T_{\rm virial}$) along the dark matter filaments into a galaxy from a wide range of distances and is dominant both in high-redshift environments and low-density environments at $z \sim 0$ (e.g., Kereš et al. 2005; Dekel et al. 2009). In contrast, hot mode accretion (i.e., gas with $T_{\rm gas} > T_{\rm virial}$) dominates in dense environments at low-redshift. A complication with this mode of accretion is that the hot gas must cool sufficiently through, for example, radiative means to $T_{\rm gas} < T_{\rm virial}$ prior to becoming integrated into the galaxy. Additionally, these two modes of gas accretion can coincide in a given galaxy.

2.1.2 Mergers

Another mechanism of galaxy growth is mergers. Galaxy mergers can be broadly categorized into two main groups: minor mergers with mass ratios of $< 4:1$ and major mergers with mass ratios of $1:1$. The contents of the merging galaxies play a large role in the outcome of the merger. A merger where both galaxies are gas-rich is often called a wet-merger and can trigger star formation during and after the merger. An intuitive inference is that gas-rich mergers occur preferentially at higher redshifts when galaxies were, on average, more gas-rich and the universe was smaller (Lin et al. 2008). Conversely, a merger where both galaxies are gas-poor is called a dry merger and, following the above, dominate in the local universe where galaxies are, on average, more gas poor than their high-redshift counterparts (e.g., Lin et al. 2008). There is the additional category of mixed-mergers in which one galaxy is gas-poor and one gas-rich.

In the occurrence of a major merger, the end result is a galaxy lacking the pre-merger structure of its counterparts such as a disk (e.g., Barnes & Hernquist 1998). In this scenario, the result is a massive elliptical galaxy. Minor mergers do not destroy the structure of the more massive galaxy in the merger, rather they are thought to be one of the major growth pathways for massive spiral galaxies (e.g., Naab et al. 2009).

Theoretical and numerical modelling is important for understanding the role of mergers in massive galaxy growth. Evidence from cosmological hydrodynamical simulations such as Illustris showcase the importance of filamentary structures corresponding to both cold-mode accretion and galaxy mergers (Sijacki et al. 2015). Figure 2.3 shows the redshift evolution of a slice of the Illustris simulation and demonstrates the importance of filamentary structures and the increasing gas density at the intersections of these filaments with decreasing redshift. This is further discussed in Section 2.2 and observational evidence on the occurrence of mergers is discussed in Chapter 3.

2.2 Galaxy evolutionary sequence

There are many proposed scenarios to explain the process of galaxy evolution; focusing on massive galaxies, here follows the description of one of the most popular, though relatively simple scenarios for the development of such galaxies. A massive

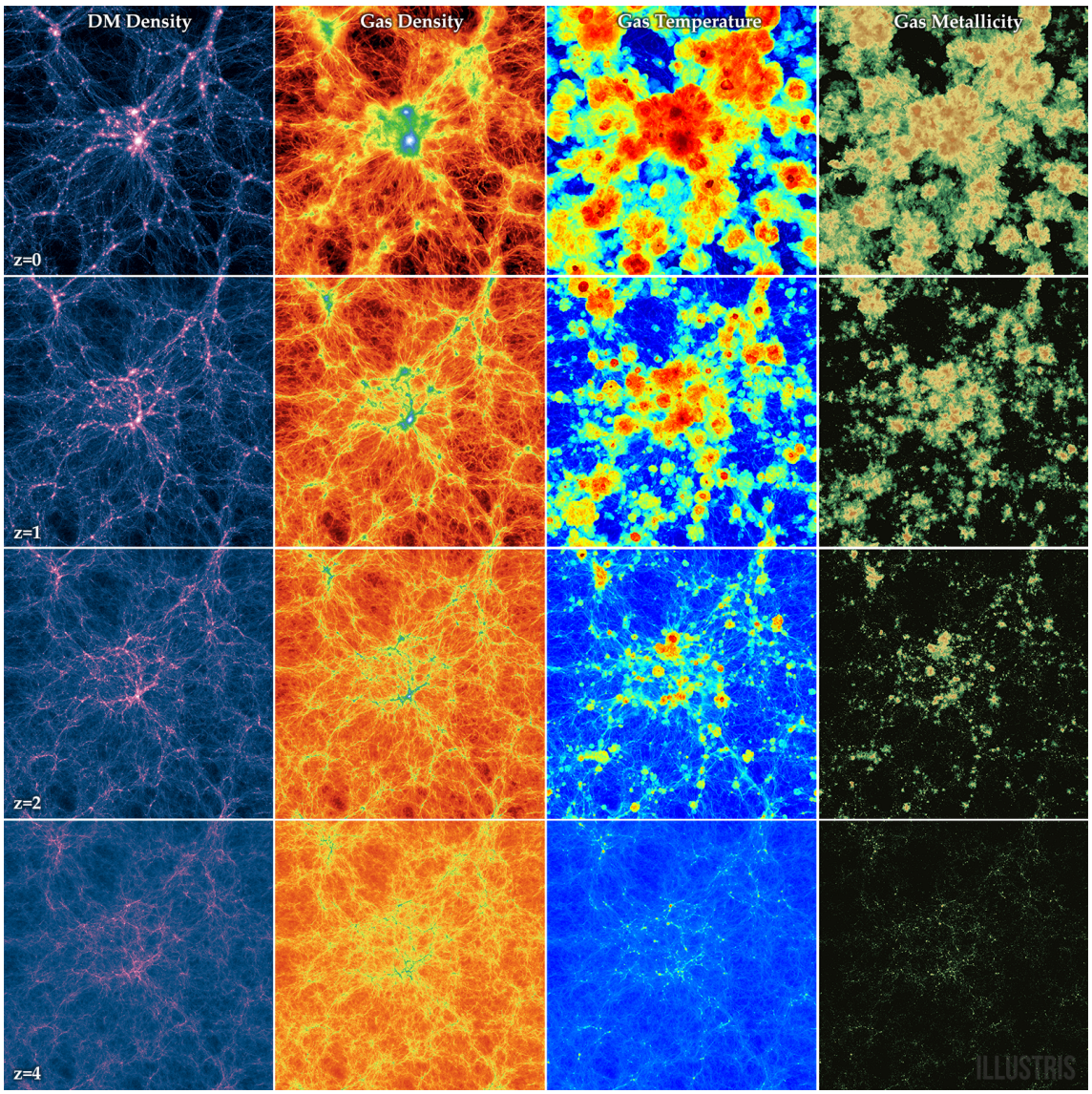

Figure 2.3: Different redshifts of a box slice of the Illustris simulation with lowest redshift ($z = 0$) at top. Columns from left to right: the dark matter density, gas density, gas temperature, and gas metallicity. It can be clearly seen that all properties increase or become more clumped together with decreasing redshift, and the importance of the dark matter structure is clear. Figure from Illustris Collaboration/Illustris Simulation.

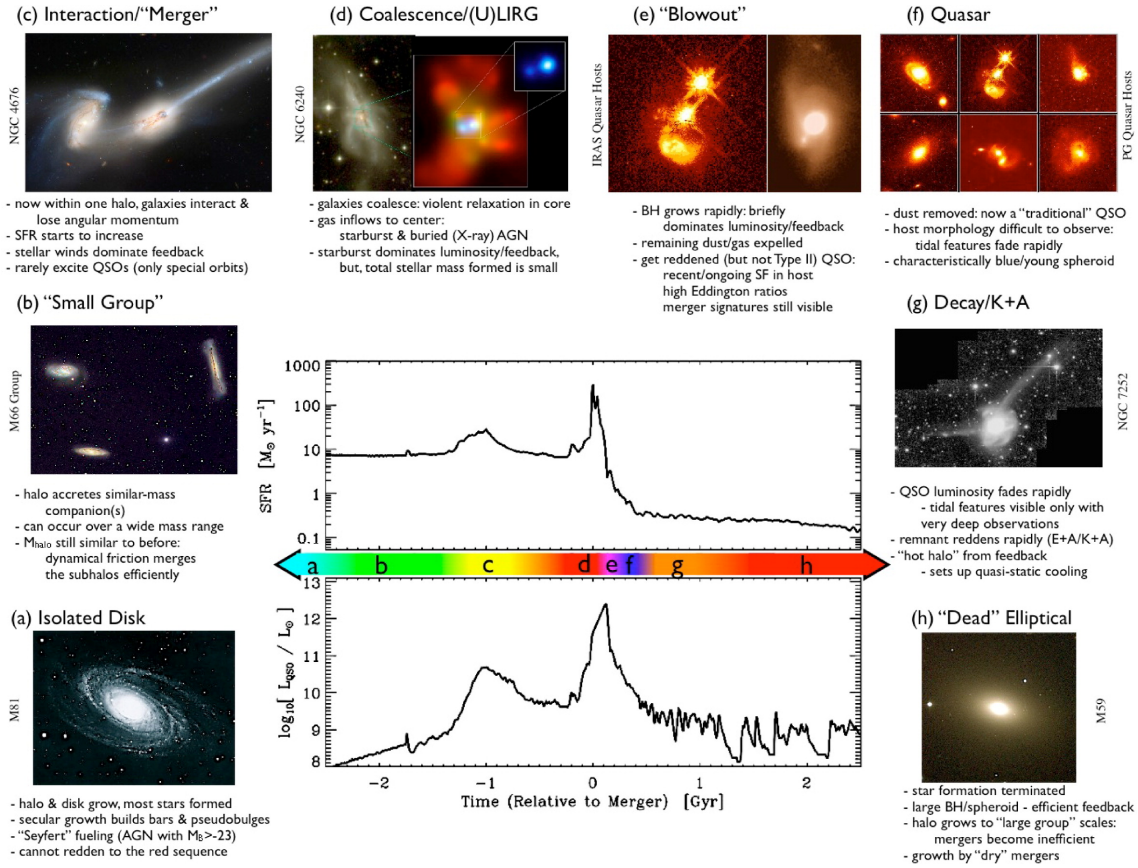

Figure 2.4: An example of the evolutionary steps of massive galaxy evolution. Note the increase in star-formation rate in top the central plot through steps d and e. Figure from Hopkins et al. (2008).

galaxy develops in an over-dense environment. This over-density easily lends itself to the galaxy undergoing merger activity, be it major or minor interactions. Following a major interaction (or an accumulation of minor ones) the galaxies coalesce together and subsequently undergo a blowout phase, during which gas and dust are ejected from the galaxy. The coalescence phase is thought to be a period in which the central SMBH grows dramatically through excess matter infall provided by the merger(s). As the gas and dust have now been blown away from the galaxy, the galaxy presents as an unobscured quasar. Eventually, the lack of matter infall on the AGN leads to quiescence of the SMBH and similarly a lack of star-formation. The already-formed stars within the galaxy gradually age and the galaxy transforms into a massive 'red and dead' elliptical galaxy (e.g., Sanders et al. 1988; Sanders & Mirabel 1996; Springel et al. 2005; Hopkins et al. 2006; Dasyra et al. 2007; Hopkins et al. 2008). This process is shown in detail in Figure 2.4.

This scenario presupposes galaxies grow in over-dense environments and that merger activity, specifically in the early universe, be high. Thus, predicting the presence of over-densities of galaxies at high-redshift is essential to verifying if this scenario is viable. Simulations of the high-redshift universe, such as Illustris (Sijacki et al. 2015) and Horizon-AGN (Dubois et al. 2014), have demonstrated the ubiquity of predicted interactions at high-redshift. Studies have shown that

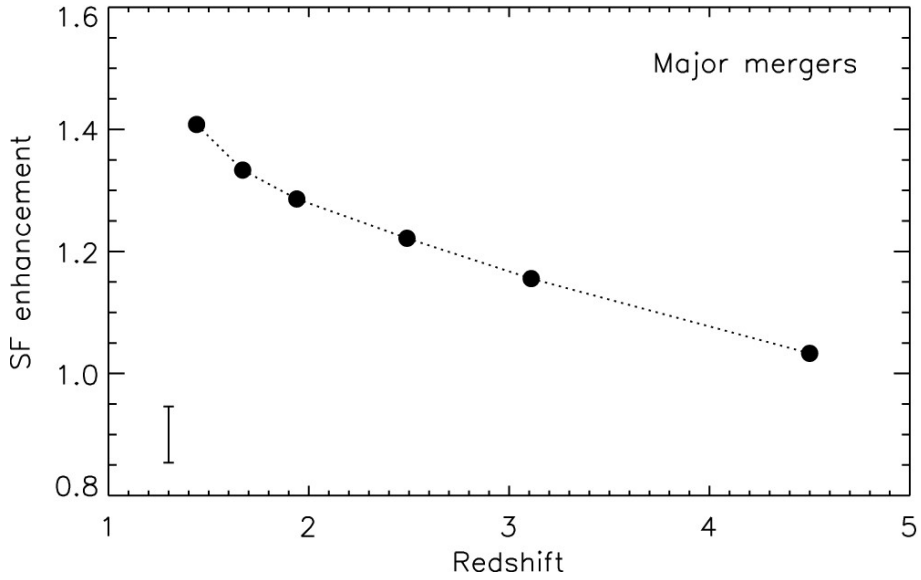

Figure 2.5: The star-formation enhancement following a major merger as a function of redshift in the Horizon-AGN simulation. The rate of enhancement drops significantly with increasing redshift. Figure from Kaviraj et al. (2015).

minor mergers affect the star-formation rates and the evolution of massive galaxies (e.g., Kaviraj et al. 2015; Sparre & Springel 2016; Pearson et al. 2019; Patton et al. 2020). By analyzing the results of the Horizon-AGN simulation, Kaviraj et al. (2015) found that by $z \sim 1$ all massive ($> 10^{10}\mathrm{M}_{\odot}$) galaxies had undergone a major or minor merger and that minor mergers were around 2.5× more common than major mergers in the redshift range $1 < z < 4$. In addition, the authors found that major mergers were, in fact, not the dominant source of star-formation enhancement in a galaxy, but rather than minor mergers claimed this responsibility (Figure 2.5). As additional corroboration, a study by Fogasy et al. (2017) used semi-analytical model simulations and set a theoretical prediction that 22% of quasars should have at least one companion with stellar mass $> 10^{8}\mathrm{M}_{\odot}$.

Direct observations of companion galaxies, specifically less massive companions, are increasingly challenging with increasing redshift. However, these challenges are being overcome and a slow but steady trickle of studies with detections of faint companion galaxies to high-redshift massive galaxies have begun to come in. These observations are further discussed in Chapter 3.

2.3 Starburst galaxies

Most star-forming galaxies in the universe follow a trend relating star-formation rate with stellar mass. This trend is generally referred to as the 'main-sequence' of star-forming galaxies (e.g., Brinchmann et al. 2004; Daddi et al. 2007; Elbaz et al. 2007; Noeske et al. 2007). Starburst galaxies lie above this trend. Their increased star-formation rates are typically attributed to the galaxy having undergone a star-formation triggering event such as galaxy interactions or mergers.

Starburst galaxies can have star-formation rates up to 1000× the rate of

typical main-sequence galaxies. A simple but relevant comparison is that of the Milky Way to local and high-redshift starburst galaxies. The Milky Way has a star-formation rate of $\sim 1-2\mathrm{M}_{\odot}\mathrm{yr}^{-1}$ and lies on the local main-sequence (e.g., Licquia & Newman 2015). M82, a local starburst galaxy, has a star-formation rate of $\sim 10\mathrm{M}_{\odot}\mathrm{yr}^{-1}$ (e.g., Gao & Solomon 2004; Förster Schreiber et al. 2003a). HFLS3, a dust-obscured starburst at $z = 6.34$, has a star-formation rate of $\sim 3000\mathrm{M}_{\odot}\mathrm{yr}^{-1}$ (Riechers et al. 2013).

2.4 Active galactic nuclei

General reference: Kormendy & Ho (2013)

Galaxies in which the nuclear region of the galaxy emits prodigious amounts of energy are called Active Galactic Nuclei (AGN). In these galaxies it is thought to be the SMBH that powers the aforementioned energy and that the luminous nature of the nuclear region is the observational aspect of this phenomenon triggered by matter infall towards the black hole. The AGN population plays a key role in suppressing star formation, especially important since the number density of known quasars peaks at $z \sim 2-3$ when galaxies were at their most gas-rich (e.g., Fabian 2012).

The observational characteristics of these galaxies are very diverse and thus there are a breadth of different categories AGN can fall into. The most popular description of this characterisation currently adopted is termed the 'unified model of AGN' (e.g., Antonucci 1993; Urry & Padovani 1995; Tadhunter 2008). This model explains the different classes of AGN as being dependent on the orientation of the galaxy with respect to the observer; any observational differences between galaxies deemed to be AGN assumed to stem from the viewing angle, shown in Figure 2.6. In this model, the SMBH is surrounded by an accretion disk of sub-pc size from which matter infalls towards the SMBH thus driving its growth. Surrounding this is a larger, obscuring, dusty torus structure located at a distance of $0.1-10\,\mathrm{pc}$ (e.g., Ramos Almeida & Ricci 2017). Jets from the SMBH are powered by the extreme amount of matter infall, pushing matter perpendicularly out of the disk.

The infall of matter onto the central SMBH is thought to be one of the primary channels through which SMBH growth occurs. A tight correlation has been found between the mass of the SMBH and the velocity dispersion (σ) of the galaxy (e.g., Magorrian et al. 1998; Ferrarese & Merritt 2000; Gebhardt et al. 2000; Häring & Rix 2004; Gültekin et al. 2009; Beifiori et al. 2012; Kormendy & Ho 2013; Bennert et al. 2015; Reines & Volonteri 2015). This suggests a co-eval evolution of the SMBH and the host galaxy and makes understanding the role of the central AGN an even more pressing matter, especially with the known decrease in AGN following cosmic noon.

In recent decades it has been shown that cosmic noon was not only a peak of cosmic star-formation, but also a peak for AGN activity (e.g., Warren et al. 1994; Schmidt et al. 1995; Kennefick et al. 1995). During this time the most massive and most luminous AGN prevailed in the universe. This also implies that AGN growth 'shut-off' after following cosmic noon. In other words, if there was no mechanism of

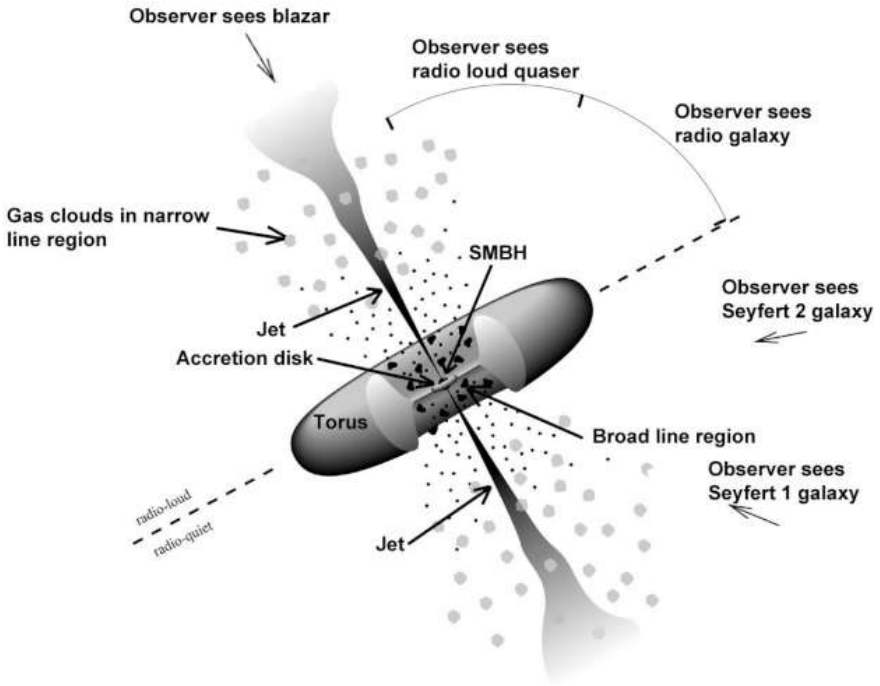

Figure 2.6: A mock-up of the unified model of AGN demonstrating their different classifications depending on viewing angle. Figure from Fermi and NASA.

'turning off' an AGN, they would continue growing alongside their host galaxies with no apparent limitations to their mass, which does not harmonize with observational results. However, a mechanism of quenching this growth must occur during cosmic noon for observations of the high-redshift universe to match what is observed in the local universe. AGN feedback has been named the likely culprit. Indeed, a central pillar of galaxy evolution simulations necessitate that in order to produce the structures seen in the local universe from their high-redshift predecessors, AGN-feedback must occur (e.g., Kauffmann & Haehnelt 2000; Granato et al. 2004; Di Matteo et al. 2005; Springel et al. 2005; Bower et al. 2006; Croton et al. 2006; Ciotti et al. 2010; Scannapieco et al. 2011). The full effect of AGN feedback is yet unknown, along with the scope of its influence on galaxy evolution as a whole; however, it is clear that feedback cannot be overlooked. AGN feedback is further discussed in Chapter 4.

2.5 Additional classifications

There exist a large diversity of galaxy classifications, far too numerous for an extensive summary in this licentiate thesis. However, a few deserve recognition due to relevance.

Submillimeter galaxies (SMGs) are a classification of high-redshift ($z \geq 2$) galaxies with properties similar to ultra luminous infrared galaxies (ULIRGs; Sanders & Mirabel 1996) in the local universe. SMGs are rare and generally faint in UV and visible light but extremely bright in sub-mm wavelengths ($> 1.0\,\mathrm{mJy}$

at 870 μm, Blain et al. 2002). SMGs are heavily dust obscured and have high infrared luminosities, typically $L_{\rm IR} \geq 10^{12} L_{\odot}$, and thus high star formation rates of $> 1000 {\rm M}_{\odot} {\rm yr}^{-1}$. In addition, these galaxies have been found to have high gas masses and gas fractions as well as high dynamical masses (e.g., Tacconi et al. 2008; Engel et al. 2010; Riechers et al. 2011; Bothwell et al. 2013). Observations of SMGs benefit from a negative K-correction[1] which results in high-redshift galaxies exhibiting similar flux at sub-mm wavelengths between $z = 1 - 8$ (e.g., Casey et al. 2013). It has been shown that the SMG population peaks at $z \sim 2.5$ (e.g., Chapman et al. 2005).

Hot dust-obscured galaxies (Hot DOGs) are a rare class of strongly obscured and dusty galaxies with very red $[3.6 - 4.5]\,\mu m$ vs. $[4.6 - 12]\,\mu m$ colors in the Wide Infrared-Survey Explorer (WISE) color-color plot. Only around 1000 of this galaxy type have been found (e.g., Eisenhardt et al. 2012), and are constrained to the redshift range $1 < z < 4$ (e.g., Wu et al. 2012; Tsai et al. 2015). The bolometric luminosities of these galaxies are extremely high, $L_{\rm bol} > 10^{13} L_{\odot}$ (e.g., Jones et al. 2014; Wu et al. 2014), and strong evidence suggests that these sources harbour strongly dust-obscured AGN (e.g., Stern et al. 2014; Piconcelli et al. 2015; Assef et al. 2015; Fan et al. 2016).

Lyman break galaxies (LBGs) are a class of star-forming high-redshift galaxies that are selected based on the presence of a characteristic break in the UV-portion of their spectrum (e.g., Steidel et al. 1996; Giavalisco 2002). The on-going star formation within these galaxies creates conditions in which significant UV light is produced from O- and B-type stars. The IGM of these galaxies absorbs the UV light at wavelengths shorter than 912 Å, thereby creating a sharp break in the galaxy's light. As redshift increases, the break also becomes redshifted, and allows for relatively easy detection with observations over a wide range of wavelengths (see Stark (2016) for a review of observations of LBGs during the reionization epoch).

Lyman-α emitters (LAEs) are a class of high-redshift galaxies that strongly emit Lyman-α from neutral hydrogen. Lyman-α emitters can be observed using narrowband imaging specifically designed to avoid the OH forest of emission lines. Detection surveys for LAEs have been extremely successful at finding high-redshift galaxies, see Stark (2016) for a review.

[1]The negative K-correction is the term assigned to the observational phenomena by which the flux density observed at wavelengths longer than 250 μm stops declining as the inverse square of distance. Instead it remains approximately constant from $1 < z < 10$.

CHAPTER 3

THE ROLE OF ENVIRONMENT: COMPANION GALAXIES

As highlighted in previous chapters, the role of a massive galaxy's environment is likely an important aspect of its evolution. Interactions between massive galaxies and their companions represent an evolutionary juncture in the evolution of these galaxies and their fate. The companion galaxies of massive, high-redshift galaxies can either be themselves massive, or be significantly smaller; interactions with the latter typically result in minor merger events. As introduced in the previous chapter, minor mergers are predicted to play an important role in the enhancement of the star-formation rate of massive galaxies in the early universe.

These predictions have prompted the search for companion galaxies, small and large, in the high-redshift universe. Direct observations of companion galaxies is a challenging task. Companions need not be as massive as their massive counterparts and might be located relatively near their massive neighbors, and thus difficult to resolve and/or distinguish at the typical resolution of observations (> 1 arcsecond). Detections of merger activity are generally associated with observations of tidal structures, direct imaging of the merger (such as the case of NGC 2623, Cortijo-Ferrero et al. 2017), or the use of kinematic signatures such as evidence of outflowing gas that can be directly associated with the companion. Combined, this has posed a great challenge in detecting companions at high-redshift, and thus complicated studies on the role of mergers as a significant factor in the evolution of distant, massive galaxies.

The angular resolution of observations depend, among other things, on the distance to the observed source. The spatial size as seen per arcsecond increases up to a redshift of ~ 2 at which point the curve turns over and begins decreasing due to the expansion of the universe and the finite speed of light, see Figure 3.1. For observations of $z \sim 4-5$ objects, the spatial size of said observations are $\sim 6-7$ kpc per arcsecond. As a reference point for galaxy structure size, the diameter of the Milky Way is ~ 30 kpc. The consequence of this is that much of the finer structure is lost in high-redshift observations. Hence, resolving massive companions from massive galaxies is a challenge, and even more so for the faint and small companions

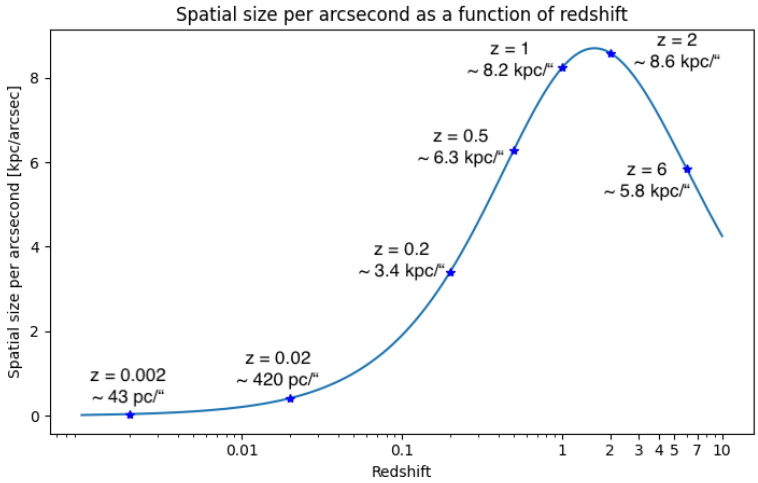

Figure 3.1: The spatial size per arcsecond as a function of redshift using Planck 2015 Cosmology (Planck Collaboration et al. 2016). Illustration by Madeleine Yttergren.

to massive galaxies.

Furthermore, the amount of time spent observing on-source greatly impacts the ability to detect fainter companion galaxies. For example, consider a scenario in which observations target the [C II] line of a massive galaxy at $z = 4.5$ and detect a peak flux density of 10 mJy and full-width-half-max (FWHM) of 300 km s^{-1} corresponding to a line luminosity of $L_{[\mathrm{CII}]} = 2.0 \times 10^9 L_\odot$ or a SFR of $\sim 180 \mathrm{M}_\odot \mathrm{yr}^{-1}$ (using the starburst relation from De Looze et al. 2014). Companions exhibiting 10% the flux density of the massive galaxy (1.0 mJy) would have line luminosities of $L_{[\mathrm{CII}]} = 2.0 \times 10^8 L_\odot$ or a SFR of $\sim 20 \mathrm{M}_\odot \mathrm{yr}^{-1}$. In order for ALMA to detect such companions with 5σ certainty in a 50 km s^{-1} channel, images would need to have resolutions of 0.2 mJy beam^{-1} per channel. This corresponds to 2 hours of on-source observing time. Changing the peak flux density of the companions to 2.0 mJy results in 30 minutes of observing time required for a 4σ detection. These hypothetical scenarios demonstrate the importance of deeper observations than what is commonly performed with the Atacama Large submillimeter/Millimeter Array (ALMA) of $\sim$ 30 minutes. However, the ability to detect companion sources also depends greatly on the tool utilized to observe them. Studies using continuum observations have often reported no overdensities around massive high-redshift galaxies (or even underdensities, e.g., Willott et al. 2005; Yue et al. 2019) while others using line emission (typically [C II] or Lyman-α) report detections of companions (e.g., Neeleman et al. 2019; Venemans et al. 2020).

Indeed, the difficulties in observing high-redshift companion galaxies has led to conflicting results, specifically when using optical, near-infrared, or Lyman-α emission. A number of studies found little evidence of companion galaxies around high-redshift starbursts and quasar host galaxies (e.g., Willott et al. 2005; Bañados et al. 2013; Mazzucchelli et al. 2017; Yue et al. 2019). For example, Bañados et al. (2013) searched for LAEs around the $z \sim 6$ galaxy ULAS J0203+0012 and concluded that there was no difference in LAE number density surrounding that galaxy in com-

parison to blank field surveys. However, other studies detected over-dense regions surrounding the galaxy of interest (e.g., Husband et al. 2015; Fan et al. 2016). For example, Husband et al. (2015) used Multi-Object Spectroscopic Explorer (MUSE) observations to investigate the environment of the quasar PKS1614+015 at $z = 3.2$. PKS1614+015 is a well-known quasar that had previously been identified as a system consisting of the radio-loud quasar and a companion galaxy with a bridge of ionized gas extending between the two sources. The MUSE observations detected this bridge in Lyman-α emission along with three other Lyman-α emitting galaxies within the virial radius of the quasar; this suggests that this system is either in the process of merging or will one day do so. These conflicting results illustrate the difficulty of drawing firm conclusions about the presence of overdensities in the environment of high-redshift massive galaxies.

In recent years, with the assistance of ALMA and other radio interferometers, the hunt for companion galaxies to massive high-redshift galaxies has become more fruitful. Observations targeting the bright and ubiquitous [C II] emission line and ^{12}CO (hereafter CO) have led to a striking increase in companion detections and indications of interaction activity (e.g., Oteo et al. 2016; Trakhtenbrot et al. 2017; Decarli et al. 2017; Díaz-Santos et al. 2018; Wardlow et al. 2018; Casey et al. 2019; Jones et al. 2019; Litke et al. 2019; Neeleman et al. 2019; Fogasy et al. 2020; Venemans et al. 2020; Bischetti et al. 2021). These studies have not only detected massive companions to massive galaxies, but have begun the onerous task of finding smaller companions and indications of galaxy-galaxy interactions. These discoveries have mainly resulted from the unprecedented imaging capabilities of ALMA at millimeter and sub-millimeter wavelengths. By taking advantage of ALMA's large array, observations of the high-redshift universe (up to $z \sim 6$) can now probe down to spatial scales sufficiently small to detect and resolve faint companions.

Indeed, Bischetti et al. (2021) studied eight $2.4 < z < 4.7$ quasar host galaxies and found that 80% had at least one companion galaxy within $\sim 6 - 120$ kpc (projected distance). The companions detected in this study exhibited CO or [C II] emission line flux similar to their quasar companion. However, one companion $\mathrm{Comp2_{J1549}}$ to the quasar J1549+1245 was found to have continuum and CO(4-3) line emission at $\sim 17\%$ the strength of the quasar.

Díaz-Santos et al. (2018) used ALMA to observe 212 μm continuum emission in the Hot-DOG W2246-0526 at $z = 4.6$. Through these observations, the authors find three faint companions around the quasar with clear indications that these companions are interacting with the quasar. Continuum observations show a dusty tidal structure between one companion and the quasar, and bridge-like structures of gas and dust between the two other companions and the quasar, shown in Figure 3.2. The dust mass in the gas bridge alone was found be to comparable to the dust mass of the three companions combined. A calculation of the velocity of the gas suggests that the sources are gravitationally bound and, similar to the quasar PKS1614+015, will be or are in the process of merging.

Another well-known example is the environment of the $z = 4.7$ quasar host galaxy BRI1202-0725. Early ALMA observations of this quasar demonstrated the telescope's remarkable observational capabilities. The quasar was previously known to be a system with a quasar and an SMG at a projected distance of 26 kpc

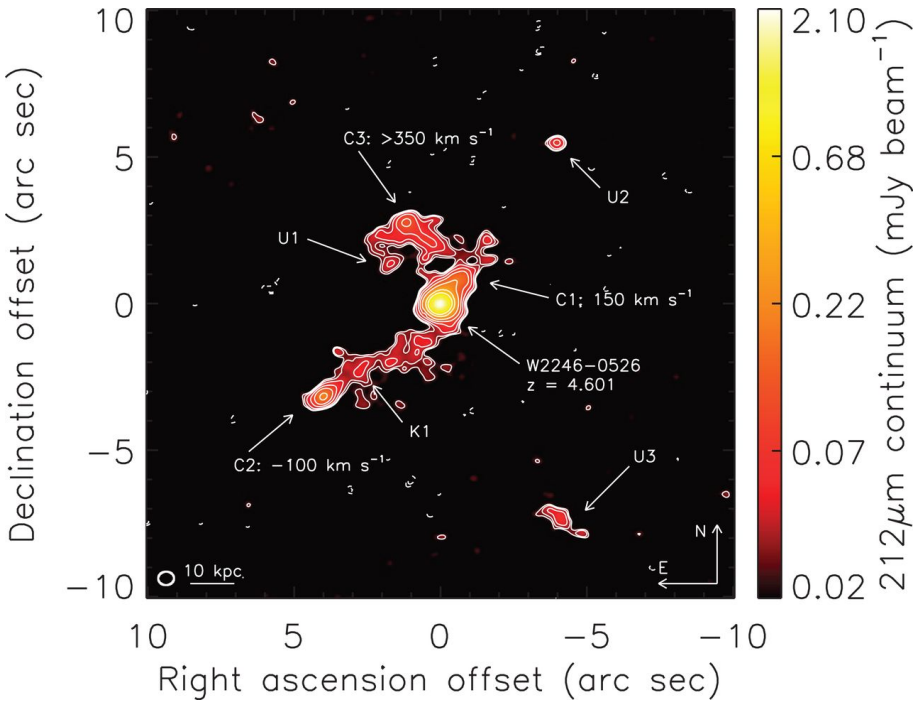

Figure 3.2: ALMA dust continuum image of the Hot DOG W2246-0526 system. The gas bridge-like structures can be seen between C1 and C2 with the central galaxy. A tidal structure is seen between C3 and W2246-0526. Figure from Díaz-Santos et al. (2018)

(e.g., Omont et al. 1996). The ALMA observations used in the study detected two additional LAEs within a projected distance of 35 kpc (Carilli et al. 2013). Additionally, the authors found evidence of a possible gas bridge between the SMG and AGN, although they note that this could be an artifact caused by one of the LAEs.

Finally, the SMG AzTEC-3 holds significance for this licentiate thesis as it is the focus of Paper I. AzTEC-3 was discovered by Capak et al. (2011) and has been extensively studied since. The system has been deemed a 'protocluster', or a massive over-dense region in the high-redshift universe. In the case of AzTEC-3, this region extends out to > 2 Mpc encompassing three Lyman-break galaxies (LBGs), one of which is thought to be composed of three smaller LBGs (Riechers et al. 2014). AzTEC-3 itself has an extreme star-formation rate ($> 1000 M_{\odot} yr^{-1}$) the implications of such a rate clearly point to possible interactions as a source of gas-enrichment (Riechers et al. 2014). In addition, observations of CO(2-1), CO(5-4), and CO(6-5) have suggested that AzTEC-3 has an unusually high-excitation gas component for an SMG, possibly caused by gravitational interactions from companions (Riechers et al. 2010).

The preceding studies have substantiated the hypothesis of companions at $z < 6$ while in fact the number of $z \sim 6$ quasars with robust interferometric studies of their characteristics and environment have also been increasing rapidly in recent years (e.g., Decarli et al. 2017, 2019; Venemans et al. 2020; Mazzucchelli et al. 2019; Meyer et al. 2022a). Venemans et al. (2020) studied 27 quasars at

$z \sim 6$ and found that 13/27 had companion galaxies within 90 kpc. Neeleman et al. (2019) used ALMA observations to categorize [C II] emission from five quasar-companion systems at $z \sim 6$. The authors calculate dynamical mass estimates from the [C II] emission in both quasars and companions; on average, the dynamical masses are similar for both types of sources. Similar to the studies from Carilli et al. (2013), Husband et al. (2015), and Díaz-Santos et al. (2018), three of these quasar-companion systems exhibited gas between the two galaxies suggestive of tidal interactions. Meyer et al. (2022a) used ALMA observations of three $z > 6$ quasars to investigate the prevalence of companions (or lackthereof).

The exact impact of the environment of high-redshift galaxies is yet to be determined, but it undoubtedly plays a major role in their evolution and star-formation. Deep, high-resolution studies with the focus of detecting the more difficult to observe faint companion galaxies will provide better constraints on the role of minor interactions and mergers. Observations of high-redshift massive galaxies with powerful interferometers such as ALMA and other next-generation telescopes currently under construction will foster the conditions under which the true extent of the effect of companion galaxies on high-redshift galaxies can be quantified.

CHAPTER 4

OUTFLOWS & FEEDBACK

General references: Fabian (2012); Heckman & Best (2014); King & Pounds (2015)

The term feedback broadly encompasses astronomical phenomena relating to the re-distribution of momentum and energy. In galaxies this takes the form of radiative and mechanical processes in which the latter generally produces outflows (although radiative feedback can also be the driving mechanism behind out-flowing material). The main drivers for these processes are thought to be star-formation driven winds, supernovae, and the central SMBH of the galaxy. The result of these effects on the contents of a galaxy have been further designated as either negative or positive feedback. Negative feedback refers to that which can suppress star formation in a galaxy, namely through driving out material or through heating the gas. Positive feedback refers to the phenomena such as jets causing star formation through their axis of propagation, as seen in Gaibler et al. (2011). It has even been proposed that star-formation occurs *within* the outflow itself, although this theory is controversial and requires additional investigation to determine its veracity (e.g., Maiolino et al. 2017; Gallagher et al. 2019). The exact role and ratio that these processes play in galaxy evolution is as of yet unknown, but their contribution is anticipated to be large.

4.1 Stellar-driven outflows

Stellar lives are energetic processes and can dramatically affect the gas and dust in the interstellar medium (ISM) of their host galaxy. Stars tend to form and live in clusters (e.g., Lada & Lada 2003; Duchêne & Kraus 2013) and the following processes are restricted to stars in this environment. Stars can drive turbulence and outflows in the following ways: protostellar outflows, stellar winds from young massive stars, core collapse supernovae, cosmic rays, radiation, type Ia supernovae, and stellar winds from old stars (e.g., Veilleux et al. 2020).

Perhaps one of the most iconic examples of this is the nearby galaxy M82. This galaxy has been called an 'archetypal example of a starburst galaxy' (Veilleux

et al. 2020). M82 has a complex star formation history and a SFR of $13-33 M_{\odot} yr^{-1}$ (Förster Schreiber et al. 2003b). A large starburst-driven outflow perpendicular to the disk of the galaxy is strongly seen in many wavelengths including X-ray and Hα optical emission with a mass loss rate of $1.4-3.6 M_{\odot} yr^{-1}$ (Strickland & Heckman 2009).

4.2 AGN-driven outflows

Outflows and feedback from AGN are an important aspect of galaxy evolution. As noted in Chapter 2.4, theoretical models require feedback to produce the properties of local galaxies. It has been suggested that AGN feedback influences the sizes of galaxies, is responsible for the steep slope of the bright end of the galaxy luminosity function, the number density of AGNs, and enriches the IGM with metals (elements heavier than hydrogen and helium; e.g., Silk & Rees 1998; Hirschmann et al. 2014; Crain et al. 2015; Beckmann et al. 2017; Choi et al. 2018; Scholtz et al. 2018). Furthermore, the effects caused by the interactions of the central SMBH and the gas within the host galaxy are thought to play a major role in regulating star-formation within said galaxy; however, the true extent of this role is unknown (e.g., Di Matteo et al. 2005; Croton et al. 2006; Harrison 2017; Cresci & Maiolino 2018; Scholtz et al. 2020).

In many simulations of galaxy evolution the gas influx in the galaxy due to an interaction is funneled into the central SMBH. Feedback effects then remove and/or heat this gas - thus regulating star-formation - through two main modes; radiative and kinetic. These two classes are based on the Eddington ratio where the radiative mode occurs preferentially at higher Eddington ratios (see Figure 18 in Heckman & Best 2014). The radiative (quasar) mode of feedback occurs in galaxies with a large reservoir of cold and dense gas in their central region. This cold gas is channeled inwards to the central SMBH, subsequently heated by the SMBH, and cooled through radiative emission.

The kinetic (radio) mode of feedback typically takes the form of powerful jets from the nuclear region of the galaxy. Gas funneled from the ISM towards the central SMBH is then ripped away by mechanical drivers, heating the gas to sufficiently high temperatures so as to prevent radiative cooling. Hence, the gas has been effectively removed from the galaxy and thus contributing to star-formation quenching.

4.3 Probes of outflows & turbulence

In the local universe, observing feedback effects and outflows from a galaxy is challenging but feasible from direct optical observations of the galaxy (e.g., M82; Strickland & Heckman 2009). In addition there are a wealth of spectral line observations that are simply unfeasible to observe at high-redshift due to their intrinsic faintness. The angular scale of possible observations at high-redshift is very limited compared to that of the local universe.

At high-redshift there are three main probes of outflows and feedback

effects: P-Cygni line profiles, observations of spectral lines associated with outflows (typically OH), and high-velocity wings on emission spectra (Figure 4.1). These probes have detected both neutral and ionized outflows in galaxies up to $z \sim 6$ (e.g., Maiolino et al. 2012; Cicone et al. 2015; Gallerani et al. 2018; Bischetti et al. 2019; Stanley et al. 2019; Ginolfi et al. 2020; Spilker et al. 2020; Butler et al. 2021). However, both have clear drawbacks as well. The use of absorption signatures such as P-Cygni profiles or OH absorption is contingent on strong continuum emission from the galaxy. The breadth of content traced by the [C II] line (through which high-velocity wings have been detected) including photodissociation regions (PDRs), neutral gas, and ionized gas, results in ambiguous conclusions about the origin of the outflow ([C II] emission is further discussed in Chapter 5.3.1.1).

In the local universe similar methods are utilized in detecting outflow signatures in galaxy spectra. However, the range of molecules available with which to detect these signatures dramatically increases. P-Cygni line profiles observed in a variety of far-infrared OH line transitions are a clear indicator of out-flowing material. The increase of tracers is best illustrated with the high velocity wings of spectra observed in local galaxies. This method has been used with CO, HCN, HCO^+, HNC, and more. Additionally, shock tracers such as SiO and methanol can be used to infer the presence of outflows.

A perfunctory measurement is the mass loading factor, $\eta = \dot{M}_{\rm out}/M_*$ where $\dot{M}_{\rm out}$ is the observed mass outflow rate and M_* is the mass of newly formed stars (proportional to the star-formation rate). This is a measure of the amount of gas that is blown out of the galaxy in relation to the amount of stars being formed and can therefore be seen as a measurement of whether star-formation quenching is ongoing. For $\eta > 1$ more mass is being removed from the galaxy than stars being formed and vice-versa for $\eta < 1$.

4.4 Observations of feedback & molecular gas outflows

4.4.1 Local universe

Observing outflows in the local universe is undoubtedly difficult, but these observations benefit from both images of the outflow and outflow signatures from spectra. Individual observations of specific galaxies can provide a detailed analysis of outflows in the studied objects while sample studies give the opportunity to characterize the properties of a population of galaxies.

Detections of high velocity wings in the spectra of galaxies in the local universe are becoming commonplace with a wide range of detections across molecular species (e.g., Feruglio et al. 2010; Alatalo et al. 2011; Aalto et al. 2012; Cicone et al. 2014). Cicone et al. (2014) used CO(1-0) observations of 19 ULIRG galaxies to conclude that although star-formation driven outflows were present and able to power massive molecular outflows, the effect of outflow enhancement from the AGN was significant.

A rather astounding example of the advantage of observing galaxies in

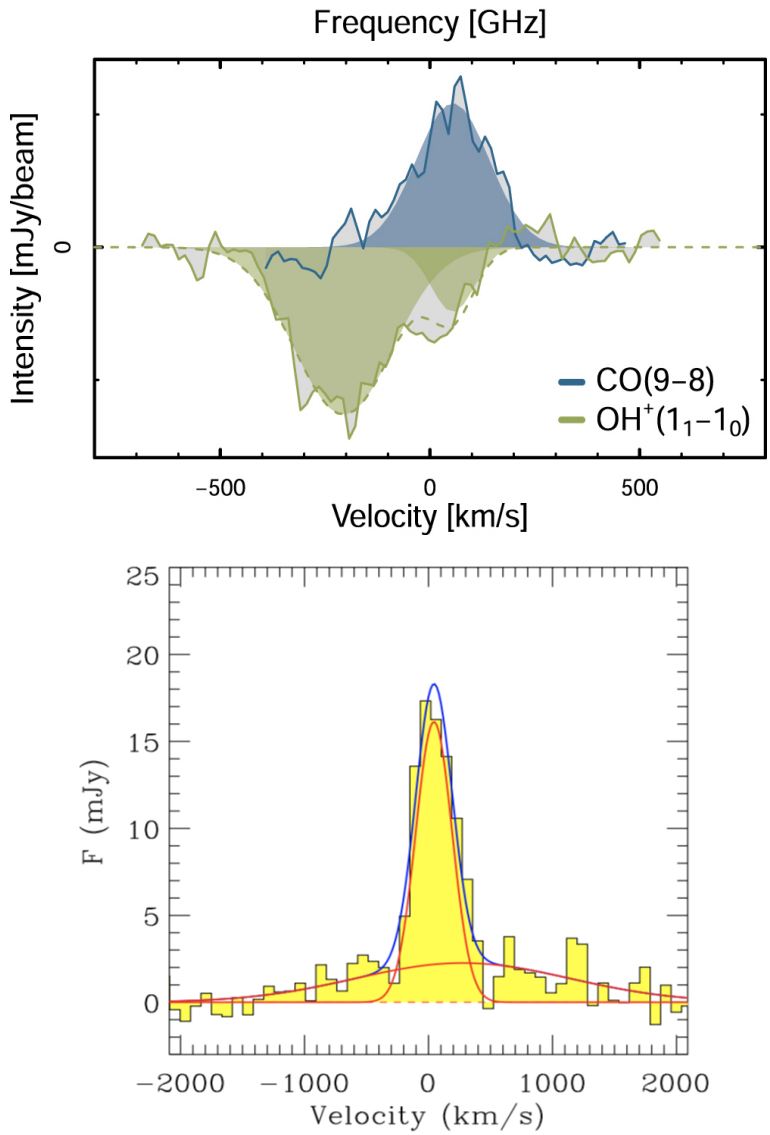

Figure 4.1: Left: Absorption line profile of OH^+ indicative of outflows in starburst galaxies, figure from Butler et al. (2021). Right: [C II] line profile suggesting a broad velocity component (Maiolino et al. 2012), though see more recent results from Meyer et al. (2022b).

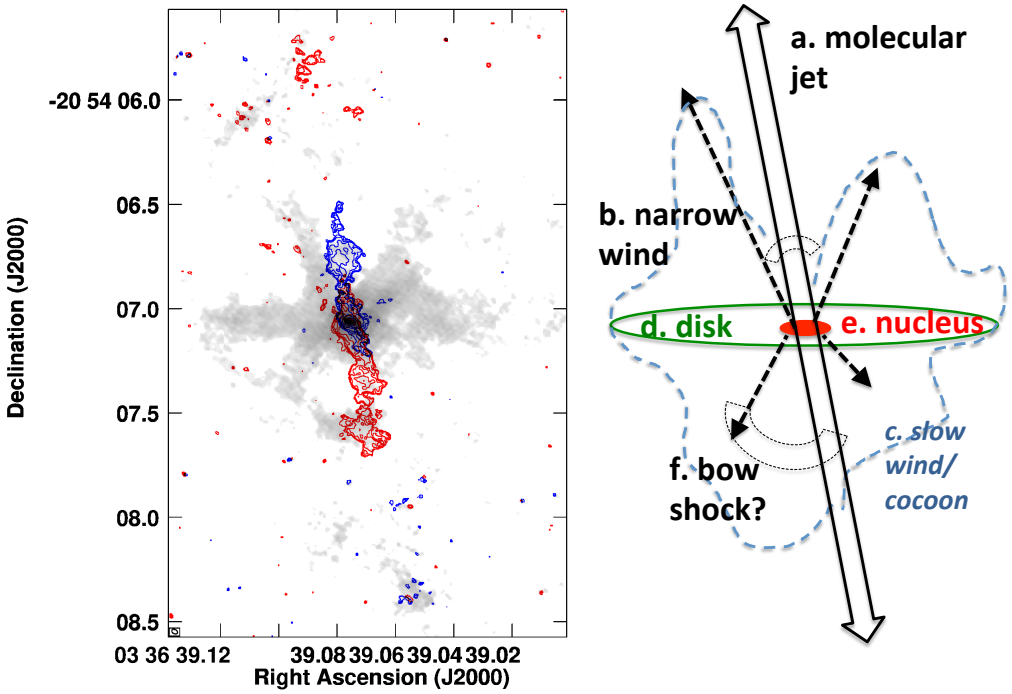

Figure 4.2: The molecular jet of NGC1377. Left: background gray shows CO(3-2) close to the systemic velocity for the source. The red and blue contours show the high velocity CO(3-2) emission in the red and blue wing of the spectra, respectively. Right: a mock-up of the components of the outflow. Figure from Aalto et al. (2020).

the local universe is that of NGC1377. Aalto et al. (2020) combined observations of CO(3-2), HCO^+(4-3), and vibrationally excited HCN(4-3) to resolve the molecular jet extending from this galaxy. This outflow presents as a collimated jet extending 150 pc from the galaxy center, shown in Figure 4.2.

4.4.2 High-redshift universe

Direct observations of outflows in the high-redshift universe are more rare than in the local universe due mainly to observational difficulties. However, the number of known detections is increasing. For example, Maiolino et al. (2012) detected an extreme outflow in the quasar SDSSJ114816.64+525150.3 (hereafter J1148) at $z = 6.4$ with a mass-outflow rate of $\dot{M}_{\rm out} > 3500 {\rm M}_\odot {\rm yr}^{-1}$ inferred from broad velocity wings found in the [C II] spectrum of the quasar. The extraordinary inferred mass outflow rate of this galaxy prompted additional studies of its properties and Cicone et al. (2015) re-estimated the mass outflow rate to be $\dot{M}_{\rm out} \sim 1400 {\rm M}_\odot {\rm yr}^{-1}$. However, with recent data of improved quality, Meyer et al. (2022b) found no evidence of the broad velocity wings in the [C II] spectra of J1148. This suggests that, for at least [C II] emission, additional factors may be at play. This is discussed in Chapter 4.5.

Spilker et al. (2020) searched for outflows using OH observations in 11 lensed dusty star-forming galaxies at $z > 4$, and found evidence of outflows in eight of these galaxies. Riechers et al. (2021a) studied starburst galaxies in the range $2 < z < 6$ and detected OH^+ emission or absorption in their sample of 18

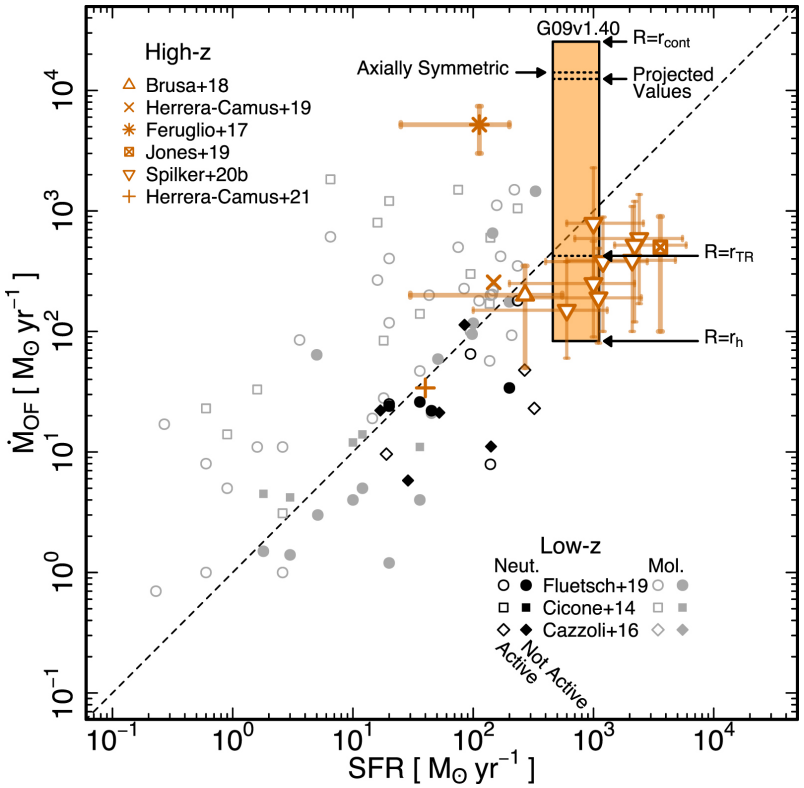

Figure 4.3: Mass outflow rate versus star-formation rate compiled from a variety of low- and high-redshift samples. The legend in the bottom right of the plot shows the known characteristics of the outflow for low-redshift samples and similar for the top right for high-redshift samples. Figure from Butler et al. (2021).

starburst galaxies and found that the majority showed feedback signatures. The authors conclude that, based on the observed velocity shifts in the line profiles of the detected emission, this emission is evidence of outflows or inflows operating within the galaxies. Riechers et al. (2021b) studied the dusty starbursting major merger ADFS-27 ($z = 5.65$) and, using detections of OH^+, concluded that a major molecular outflow was occurring within the galaxy. Butler et al. (2021) studied the star-forming galaxy HATLAS J085358.9+015537 (G09v1.40, $z = 2.09$) and, through detection of OH^+, determined that the galaxy hosted a neutral gas outflow with a mass outflow rate of $83 - 25,400 M_\odot yr^{-1}$. A compilation of molecular and neutral low- and high-redshift outflows from Butler et al. (2021) is shown in Figure 4.3.

Searches for outflows in the high-redshift universe have also utilized stacking methods, primarily through observations of the [C II] line, to amplify the signatures of outflows in less extreme objects. These approaches have led to conflicting conclusions. Gallerani et al. (2018) used ALMA observations of the [C II] line in nine galaxies at $z \sim 5.5$ with SFRs of $\sim 30 M_\odot yr^{-1}$ and found an average inferred mass outflow rate of $\dot{M}_{out} = 54 \pm 23 M_\odot yr^{-1}$. Bischetti et al. (2019) and Stanley et al. (2019) present additional detections of outflows detected through stacking procedures of the [C II] line in galaxies at $z > 4$. However, Decarli et al. (2018) performed a stacking approach of [C II] in 27 quasars at $z > 5.9$ and found no evidence for outflow signatures in their line profiles.

4.5 Interpretation of observations

An additional important consideration in studying high-redshift outflows is the nature and origin of the outflow signature. Due to limited angular resolution at high-redshifts and the methodology of detecting feedback effects and outflows it remains unclear to what extent observations have actually traced these phenomena. The commonly used approaches for detecting outflows described above can be used regardless of the angular resolution - i.e., if broad velocity wings are detected in the integrated [C II] (or other line) spectra for an entire galaxy this is typically attributed to an outflow signature. This leaves much room for interpretation of the source of this line profile feature. On the other hand, P-Cygni line profiles or lines known to be associated with outflows present a much more robust method of outflow determination in part due to the fact that the blue-shifted segment of the spectrum in P-Cygni profiles can be undeniably attributed to out-flowing gas.

The use of [C II] as a tracer of out-flowing gas has been contentious for quite some time. This was specifically called into question following the results of Spilker et al. (2020) which did not find broad velocity wings in the [C II] spectra of their studied galaxies for which they had robust outflow detections from OH spectra. There are two easily discernible explanations for this discrepancy. The first being that it is possible previous studies which detected broad velocity [C II] emission in truth originated from an insufficient continuum subtraction prior to analysis of the line spectrum. This is unlikely to be the full explanation. However, it is possible that this, combined with the possibility that the [C II] line spectrum for a given galaxy could be contaminated by as of yet unknown faint or unresolved companion galaxies, could provide a more comprehensive explanation. Indeed, Gallerani et al. (2018) note that it is possible a portion of the excess line flux they attribute to outflow signatures could be due to faint satellite galaxies. Additional substantiation to the possibility of outflow signatures being biased by continuum subtraction is the case of J1148. New observations of J1148 from Meyer et al. (2022b), again using the Northern Extended Millimeter Array (NOEMA) but with increased coverage due to a higher number of antennas, of [C II] emission in the quasar did not demonstrate a need for the broad velocity component previously found; thus implying that outflow signature was immaterial for J1148 (Meyer et al. 2022b).

A final consideration is the overall effect of the outflow on the galaxy; that is to say, is there observational evidence of a significant alteration to the state of the galaxy by the outflow? For example, Scholtz et al. (2020) found no evidence of an instantaneous effect from ionized gas outflows in a sample of moderately luminous AGN between $z = 1.4 - 2.6$ (see also Scholtz et al. 2021; Lamperti et al. 2021). The authors suggest two possible explanations for this. Firstly, that the outflow does have an effect, but that effect is limited to spatial scales smaller than those they resolved ($< 5\,\mathrm{kpc}$). Secondly, that the effect of the outflow can only be seen on longer timescales. Regardless of the explanation, their findings exemplify the need for additional studies on the effect on the host galaxy, origin of the outflow, and veracity of previous outflow observations.

CHAPTER 5

METHODOLOGY

5.1 Radio interferometry

General Reference: Wilson et al. (2013); Thompson et al. (2017)

Typical optical and single-dish radio telescopes are limited in resolution by their light collecting area - generally the diameter of the telescope. Hence, the angular resolution of these observations can be found by the simple relationship between the diameter of the telescope and the wavelength of the observation: $A_{\mathrm{R}} \propto \lambda/D$ where A_{R} is the angular resolution, D is the diameter of the telescope, and λ is the observed wavelength. An obvious consequence of this relation is that for longer wavelengths of light a much larger telescope diameter is required to obtain similar angular resolution of that possible for shorter wavelengths. Radio interferometry is a method designed to overcome this limitation.

Modern interferometry works through a process called aperture synthesis to combine signals from radio dishes in a given array to increase angular resolution according to $A_{\mathrm{R}} \propto \lambda/L$ where L is the longest distance between two radio dishes. Thus, the angular resolution of interferometric radio observations is limited by the largest spacing between antennas in an array rather than any individual antenna diameter.

Aperture synthesis synthetically increases the apparent resolution by sampling the radiation field within the desired observation area using different pairs of telescopes or baselines. The sampling from each telescope pair, called visibilities, can be expressed as the following:

$$V_{j,k}(t) \propto \int_{sky} I(\vec{\sigma}) e^{\frac{-2\pi i}{\lambda} \vec{B_{j,k}} \times \vec{\sigma}} \, d\Omega, \tag{5.1}$$

where $V_{j,k}(t)$ is the visibility for telescopes j and k at time t, $I(\vec{\sigma})$ is the source brightness function, $\vec{\sigma}$ is the position vector, and $\vec{B_{j,k}}$ is the distance between the two dishes. The position vector, $\vec{\sigma}$, is typically constructed using a coordinate system designated by (l, m) and visibilities as:

$$\vec{B_{j,k}} \times \vec{\sigma} = \lambda(lu + mv) \tag{5.2}$$

such that the visibilities are then expressed in (u, v) space. This allows us to rewrite equation 5.1 as

$$V_{u,v} \propto \int_{sky} I(l, m) e^{2\pi i(lu+mv)}\, dl\, dm, \tag{5.3}$$

which is the standard 2D Fourier transform form of the visibility equation. Finally, we can invert this equation to write it as the following:

$$I(l, m) \propto \int V(u, v) e^{-2\pi i(ul+vm)}\, du\, dv \tag{5.4}$$

where $I(l, m)$ is the intensity function for a given position (l, m). The (l, m) plane refers to the image-plane and positions in the (u, v) plane refer to the uv-plane. It should be noted that there are two caveats to these equations. First, that the number of dishes in an array is not infinite and thus the sampling of the (u, v) space is limited to the number of samples as N×(N-1) where N is the number of dishes. Second, since each dish pair must have some distance between the two, the center of phase space, $u = v = 0$ remains unsampled, along with distances less than the smallest distance between two dishes. An example of uv-plane sampling is shown in Figure 5.1.

5.1.1 Radio imaging techniques

Since scientific analyses are typically performed in the image-plane, an efficient and user-friendly algorithm must be used to sample $I(l, m)$ for any given position in the observation. The most common method is by using an algorithm called the fast-Fourier transform (FFT). FFTs sample the uv-plane at regular intervals and convolve the sampling with the interval over which the sampling occurred and output a 'dirty-image' of $I(l, m)$. This dirty-image must then undergo a deconvolution process, typically CLEAN (Högbom 1974). CLEAN, and others of its kind, are designed to correct for insufficient sampling of the uv-plane.

An important aspect of imaging is the weighting process. Specific weights can be assigned to different visibilities with the main goal of improving uv-plane sampling (however, this process can also be useful when accounting for different noise variations or improving an uv-dataset's sensitivity to extended structures or to improve resolution). The default weighting used by algorithms such as CASA's [1] TCLEAN is natural weighting which weights the data equally. Images using this algorithm have the best signal-to-noise ratio but have poorer angular resolution. Alternatively, uniform weighting assigns weights to the visibilities to ensure the uv-plane is regular (typically carried out by weighting the longest baselines as these are the least sampled). An additional weighting scheme (utilized for analysis in this licentiate thesis) is Briggs weighting. Briggs weighting is a compromise between natural weighting and uniform weighting where an adjustable parameter called the

[1] Common Astronomy Software Applications (CASA) is a software designed specifically to process interferometric data from telescopes such as ALMA or the VLA.

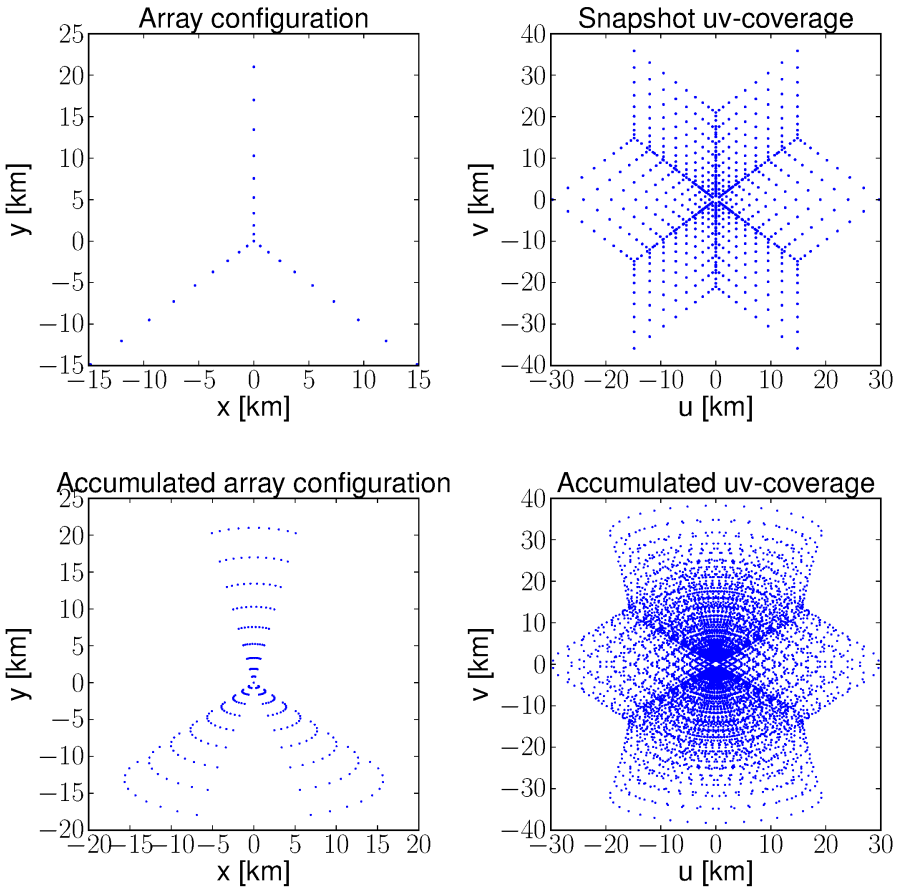

Figure 5.1: An example of a VLA configuration and the *uv*-coverage from that configuration as a snapshot, and accumulated array configuration and *uv*-coverage after 6 hours of integration including the increase in *uv*-plane sampling due to Earth's rotation. Figure courtesy of Lukas Lindroos.

robust factor varies between +2 and −2 and dictates the user's preference of being closer to uniform or natural weighting.

If a given observation is targeting an emission or absorption line, the continuum emission must be subtracted prior to determining the line flux. For ALMA observations this is typically done using CASA's UVCONTSUB task. This task works by determining a fit for the underlying continuum emission using a polynomial of order n where n is specified by the user and fitting to emission line-free channels in the observation. Generally, a polynomial fit of $n = 1$ is sufficient to remove continuum.

5.1.2 Radio interferometers

In the past decades a number of prestigious radio interferometers have come on-line, providing the scientific community with many previously impossible discover-

ies. These consist mainly of the Very Large Array (VLA) in New Mexico, USA, the Northern Extended Millimeter Array (NOEMA) in the French Alps, the Atacama Large submillimeter/Millimeter Array (ALMA) in the Atacama desert in Chile, the Low Frequency Array (LOFAR) with antennas located mainly in the Netherlands but also around the world, and more. The next-generation of ratio telescopes include the Square Kilometer Array (SKA) and the South African MeerKAT telescope.

5.1.2.1 ALMA

The observational power of ALMA is incredibly important for studying high-redshift galaxies. The different antenna configurations can reach down to arcsecond and sub-arcsecond resolutions, comparable to optical and near-infrared observations. The synthesized large collecting area made possible through interferometry means that rather than being limited to observing the most luminous high-redshift galaxies, ALMA can also probe down to more normal galaxy populations. The large spectral coverage means that far-infrared emission lines in high-redshift galaxies are redshifted into the frequency bands of ALMA receivers. These lines are essential for determining the interstellar gas properties. Combined, it has now become possible to image the structure and environment of galaxies at many different evolutionary stages.

ALMA is composed of 66 radio antennas located in the Atacama Desert in Chile at an elevation of $\sim 5000\,\mathrm{m}$ above sea-level and is shown in Figure 5.2. The Atacama desert is one of the driest places in the world and is thus ideal for radio interferometers sensitive to water vapor in the atmosphere. The telescope has two constituent arrays; fifty 12-meter dishes constitute the main observational array and the Atacama Compact Array (ACA) is made up of twelve 7-meter dishes and four 12-meter dishes. ALMA's dishes are on tracks upon which they can be moved to create different configurations and thus sample the *uv*-plane in a variety of ways. By exploiting its phenomenal observational capacity, observations with ALMA can, at the highest frequencies, reach down to spatial resolutions of 10 milliarcseconds, five times better than *Hubble Space Telescope (HST)* observations. ALMA will be the scientific workhorse of the community for years to come.

5.2 Gravitational lensing

Gravitational lensing is a natural phenomena first predicted by Albert Einstein in 1936 and confirmed in 1979. Since then it has become an essential tool in observations of high-redshift galaxies and effectively acts as a magnifying glass on faint objects.

A galaxy is said to be gravitationally lensed when it lies directly along the line-of-sight behind a more massive intervening object, such as a massive galaxy or galaxy cluster. The light from the distant galaxy is redirected around the intervening object and consequently distorted prior to reaching the point of observation. A schematic of this is shown in Figure 5.3. Gravitational lensing also has the advantage of preserving the surface brightness of the lensed galaxy while the magnification appears to make it look larger and hence brighter. This means that the physical

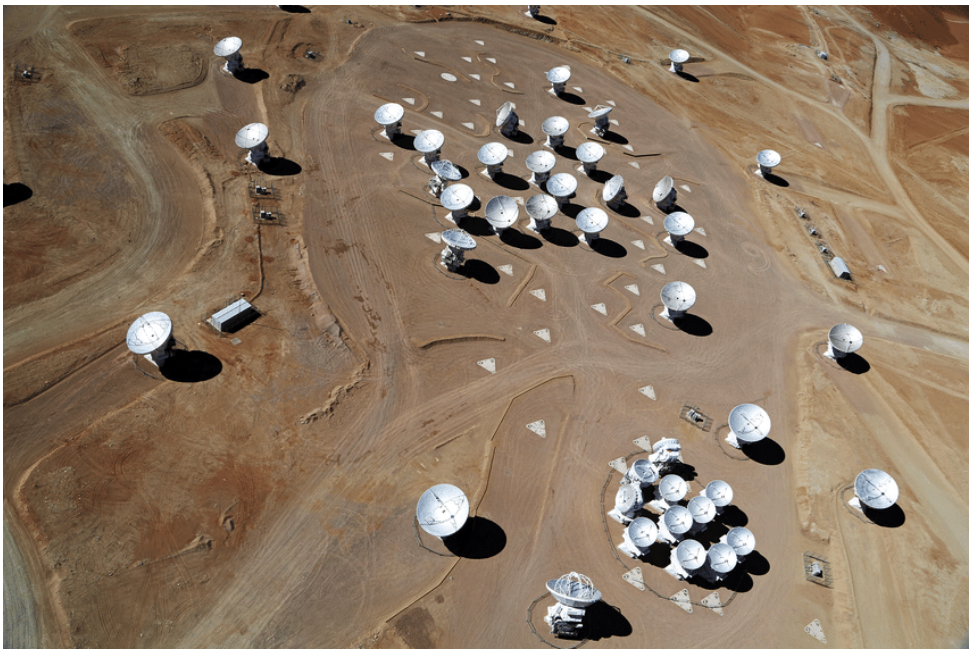

Figure 5.2: Aerial view of the ALMA telescope in the Atacama desert. Most dishes in the image are 12m main-array antennas while the small cluster in the lower right corner are the 7m dishes of the ACA. Figure from ESO.

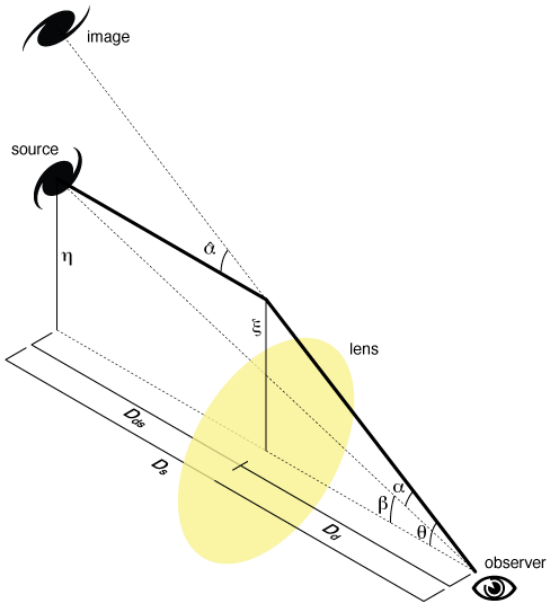

Figure 5.3: Figure demonstrating gravitational lensing. The foreground lens is shown with the yellow ellipse. The image refers to the image observed while the source refers to the true location and origin of the flux. Figure from CC BY-SA 3.0

properties of the lensed galaxy can still be studied in depth by simply correcting the brightness for the magnification factor (i.e., how many times brighter the galaxy appears). This factor can be calculated using Figure 5.3 and described with the following equation:

$$\mu = \mid \det(\frac{\partial \beta}{\partial \theta}) \mid^{-1} . \tag{5.5}$$

where μ is the magnification factor, β is the angle from the observer to the source-plane image, and α is the angle from the source-plane image to the image-plane image. Alternatively, this can be expressed as the following:

$$\mu^{-1} = (1 - \kappa)^2 \times (1 - g^2), \tag{5.6}$$

where κ is the convergence and g is the reduced shear defined as $\frac{\gamma}{1-\kappa}$ where γ is the shear. If $g = \pm 1$ this implies an infinite magnification factor along the so-called critical lines which take the form of two non-intersecting lines in the image plane. In the source plane these lines are called caustic lines and can intersect. The location of the galaxy in the source plane relative to these lines determines the location of the lensed image(s) of the galaxy in the image plane, as seen in Figure 5.4.

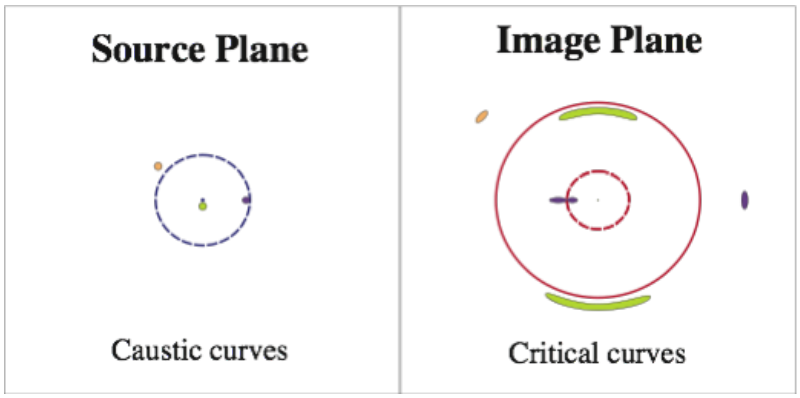

Figure 5.4: The critical and caustic curves from modelling a single circular lens. The left panel shows the source plane in which the blue dashed line is the caustic curves and the different colored blobs represent locations of flux from a source such as a distant galaxy. The right panel shows the image plane in which the red solid and dashed lines represent the critical lines and the blobs and extended arcs show the location of the resultant flux post-lensing in the source plane of the background object. Figure from Futamase (2015).

In order to calculate the magnification factor of a galaxy it is necessary to establish a mass model of the foreground source, be it a massive galaxy or galaxy cluster. This mass model uses information about the foreground mass(es) in tandem with how the background source(s) light is distorted to determine the magnification across a specified region. In studies of individual high-redshift galaxies, strong gravitational lensing (meaning lensing that produces double images or an Einstein ring) occurs primary through galaxy-galaxy lensing or lensing of a galaxy by a massive galaxy cluster. In the galaxy-galaxy lensing scenario, which is the case for the quasar BRI0952-0115 of this licentiate thesis, a single massive galaxy is located in

the foreground of the distant object. In the most extreme cases, the intervening mass causing the lensing is a galaxy cluster. In the occurrence of cluster lensing the magnification factor can be extreme; however, the mass model used to describe the gravitational lensing will be extremely complex due to the large number of galaxies involved. Magnification factors of up to $\mu \sim 30$ have been observed resulting from cluster lensing (e.g., Ebeling et al. 2018).

5.3 Probing the ISM of high-redshift galaxies

General reference: Carilli & Walter (2013)

The ISM of high-redshift galaxies provides key clues to the ongoing evolutionary processes within them and a guide for characterising them. The difficulties associated with observing high-redshift objects require unique and innovative methods of study. Attempts to study the faint emission lines and small spatial structures that can be resolved at lower redshifts are simply futile enterprises in the high-redshift universe. Only a few facilities are robust enough to detect, much less produce high quality images of, attributes of the ISM in these galaxies. This subchapter summarizes some of the tools available to study the ISM of high-redshift galaxies.

5.3.1 Atomic tracers

There exist a number of atomic tracers that are commonly used in studies of the ISM. The following two are fine structure carbon lines and are discussed due to their relevance to Paper I.

5.3.1.1 [C II] Emission

The fine-structure [C II] 158 μm ($^2P_{3/2} \rightarrow^2 P_{1/2}$) emission line is one of the most commonly used tracers of gas in high-redshift galaxies due to its ubiquitous and bright nature. This line is one of the primary coolants in star-forming regions of the ISM owning to the fact that the ionization energy required to form [C II] is 11.3 eV, lower than that of HI at 13.6 eV (e.g., Stacey et al. 1991, 2010; Carilli & Walter 2013). [C II] emission traces both the cold neutral medium and photodissociation regions (e.g., Stacey et al. 1991). Stacey et al. (2010) suggested that, at high-redshift, [C II] emission originates primarily in PDRs in star-forming galaxies.

Observations of [C II] are strategic not only because there is a high chance of detecting the line but also because its frequency is advantageous for high-redshift observations using ground-based radio facilities such as ALMA, VLA, or NOEMA. For these reasons, [C II] observations are typically the primary line emission observation carried out for galaxies at $4 < z < 7$. The wealth of observations of this line have shown that there exists a deficit in this line with respect to a galaxy's far-infrared (FIR) luminosity: [C II] line luminosity decreases with increasing FIR luminosity (e.g., Díaz-Santos et al. 2013). This deficit has been the cause of much debate since its discovery with, as of yet, no conclusion. Possible explanations in-

clude the physical scale of star formation, optical depth effects, saturation of the [C II] line, an increase in dust charge in the ISM, and AGN activity (Casey et al. 2014, and references therein). It has also been suggested that this deficit occurs preferentially in AGN host galaxies (e.g., Stacey et al. 2010). This deficit has been detected in a number of other fine structure lines (e.g., [N II], [N III], [O I], [O III]) at high redshift (e.g., Graciá-Carpio et al. 2011; Decarli et al. 2012; Farrah et al. 2013), suggesting that a systematic decrease in fine structure line emission with increasing FIR luminosity is occurring.

[C II] has also been suggested as a star-formation rate tracer with the possibility to be unbiased towards dust extinction as SFRs calculated from infrared luminosities tend to be (Lagache et al. 2018). This method has the caveat of depending strongly on metallicity (e.g., Vallini et al. 2015; Olsen et al. 2017), which can be equally difficult to categorize at high-redshift. Additionally, [C II] has recently been shown to be an inaccurate tracer of star formation in heavily obscured galaxies (e.g., Dwek & Arendt 2020). De Looze et al. (2014) studied the relationship between [C II] line emission and SFR for a variety of galaxy types in the local and high-redshift universe and determined correlations between the two depending on classification. This is rapidly becoming a common method of comparison at high-redshift for SFRs inferred from [C II] emission and those inferred from SED fits and infrared luminosities.

5.3.1.2 Atomic carbon

There are two optically thin fine structure atomic carbon transitions that, when observed together, allow for the derivation of excitation temperature, neutral carbon column density, and mass independently of other line observations. These lines, [C I] ($^3P_1 \rightarrow ^3 P_0$) and [C I] ($^3P_2 \rightarrow ^3 P_1$) (hereafter [C I] (1-0) and [C I] (2-1)), have been shown to trace CO(1-0) emission as the critical density for both is similar, $n_{\rm cr} \approx 10^{-3}\,{\rm cm}^{-3}$; thus [C I] lines provide a method for tracing total molecular gas in a galaxy when CO(1-0) is unobservable due to its faintness or thought to be underestimated due to CO-dark gas (see Hodge & da Cunha 2020, and references therein). In cases where CO(1-0) and [C I] (1-0) emission are observed, these lines can be combined to confirm the $\alpha_{\rm CO}$ conversion factor (further discussed below; e.g., Cicone et al. 2018). In addition, the [C I] (2-1) line's emission frequency is very close to that of CO(7-6), which allows many CO surveys to obtain observations or constraints to the line without additional observation time. Studies using [C I], often in combination with other CO lines, have become increasingly commonplace for galaxies in both the local- and high-redshift universe (e.g., Walter et al. 2011; Krips et al. 2016; Cicone et al. 2018; Andreani et al. 2018a; Emonts et al. 2018).

There is sparse evidence showing that the properties of these lines evolve with redshift or with galaxy type (e.g., Gerin & Phillips 2000). When observed at very high-redshifts, this line is less contaminated by both the CMB and less sensitive to cosmic rays (e.g., Zhang et al. 2016; Andreani et al. 2018b). The [C I] gas mass of the galaxy can be calculated using the following equation from Weiß et al. (2003):

$$\mathrm{M_{CI}} = 4.566 \times 10^{-4} \mathrm{Q(T_{ex})} \frac{1}{5} \mathrm{e}^{\mathrm{T_2/T_{ex}}} \mathrm{L'_{CI(2-1)}} \tag{5.7}$$

where $Q(T_{\rm ex}) = 1 + 3e^{-T_1/T_{\rm ex}} + 5e^{-T_2/T_{\rm ex}}$ is the partition function, $T_1 = 23.6\,\mathrm{K}$ and $T_2 = 62.5\,\mathrm{K}$ are the respective excitation energy transitions of the [C I] (2-1) and [C I] (1-0) lines, and T_{ex} can be taken as the ratio of the two line transitions (e.g., Jarugula et al. 2021). The total molecular hydrogen mass can then be derived from $\mathrm{M_{CI}}$ by assuming a ratio of [C I] to H_2 typically using a template source (e.g., Weiß et al. 2003; Walter et al. 2011; Jarugula et al. 2021).

5.3.2 Molecular tracers

5.3.2.1 CO spectral line energy distribution

The ^{12}CO line J-transitions have long been the most commonly used probe of the ISM in both local and high-redshift galaxies. Different J-transitions trace different gas conditions and the CO spectral line energy distribution (SLED), or CO excitation ladder, is a powerful tool for analyzing the excitation sources within a galaxy. In addition, different categorizations of galaxies, such as SMGs, seem to have characteristic CO SLEDs that can be used to infer qualities about the galaxy class as a whole.

Low-J ($J < 4$) transitions are typically produced by excited gas in molecular clouds. Specifically, the CO(1-0) line allows for a determination of the bulk density of the molecular gas content in a galaxy through a conversion factor termed $\alpha_{\rm CO}$ as $\mathrm{M_{mol}} = \alpha_{\rm CO} \times L_{\rm CO}$ where $L_{\rm CO}$ is the CO line luminosity in units of $\mathrm{K\,km\,s^1\,pc^2}$; thus $\alpha_{\rm CO}$ can be considered a mass-to-light ratio (e.g., Bolatto et al. 2013). This conversion factor is especially important due to the fact that H_2 has no permanent dipole moment making it essentially impossible to observe and thus determine its mass. This method has become contentious in past years, especially for high-redshift galaxies due to its dependence on observations of the ground state CO(1-0) line which is onerous to observe at high-redshifts. Mid-J ($4 \leq J \leq 8$) transitions occur in warm molecular gas typically through excitation by UV photons in PDRs by OB type stars. High-J ($J \geq 9$) transitions typically require more extreme forms of excitation such as AGN activity.

CO SLEDs can be categorized by their peak, or which J-transition is brightest. Rosenberg et al. (2015) studied 29 LIRGs and ULIRGs in the local universe and found three typical CO-SLED classes. Class 1 peaks at CO(5-4), class 2 at CO(7-6), and class 3 exhibits a flat CO-SLED. At higher redshifts galaxies can peak at even more extreme CO transitions (e.g., Weiss et al. 2007).

Detections of high-J CO (J>10) lines have become increasingly common at high-redshift, and continues to increase (e.g., Gallerani et al. 2014; Li et al. 2020; Jarugula et al. 2021). Perhaps the most extreme of these is Gallerani et al. (2014) who detected CO(17-16) in the quasar J1148 at $z = 6.4$. Through radiative transfer modelling the authors determined that a PDR + X-ray dominated (XDR) model of the ISM was needed to generate such intense radiation fields (see Figure 5.5), thus providing evidence of the AGN's (the likely origin of the XDR) direct influence on the ISM.

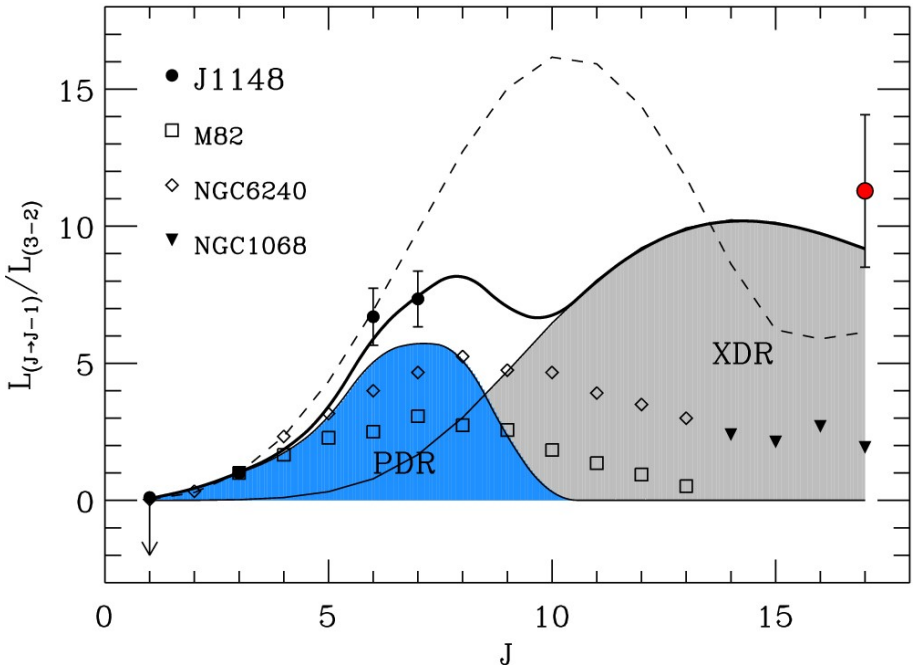

Figure 5.5: The CO SLED of the quasar J1148 and other local galaxies. The blue region under the black curve represents the flux which can be accounted for using PDR modelling and the shaded grey region represents that which required XDRs to produce. Figure from Gallerani et al. (2014).

5.3.2.2 Water

Studies targeting water lines in galaxies at both low- and high-redshift have shown that, in the warm, dense, star-forming and shock-heated regions of the ISM, water is the third most abundant molecule (e.g., Bergin et al. 2003; Cernicharo et al. 2006; González-Alfonso et al. 2013) and a prime candidate for gas excitation studies. Water is divided into ortho- and para-transitions depending on the spin of the hydrogen atoms, and an important consequence of the nature of this division is that different water molecules are constrained to transitions only within the division the molecule belongs to (i.e., either ortho or para).

Liu et al. (2017) performed a detailed study of water lines in galaxies at $z < 1$ and combined these observations with radiative transfer modelling to link different water transitions to different regions of the ISM based on temperature. Through these links the authors predicted line excitation intensities throughout the ISM, shown in Figure 5.6. The authors found that lines such as the H_2O $(2_{12} - 1_{01})$ transition are very bright in the cold, dense, extended region of the studied galaxies due to strong collisional excitation. Lines such as H_2O $(2_{02} - 1_{11})$ were found to be bright in both the warm and hot components of the ISM, but least affected by radiative pumping within the galaxy. In the warm, dense, and star-forming regions of the ISM young O- and B-type stars contribute heavily to UV radiation production, producing H_2O $(3_{12}-3_{03})$. The authors found that the H_2O $(3_{21}-3_{12})$ line was bright in both the warm and hot components of the ISM due to its ability to be excited through either collisional and radiative means. Finally, higher energy transitions

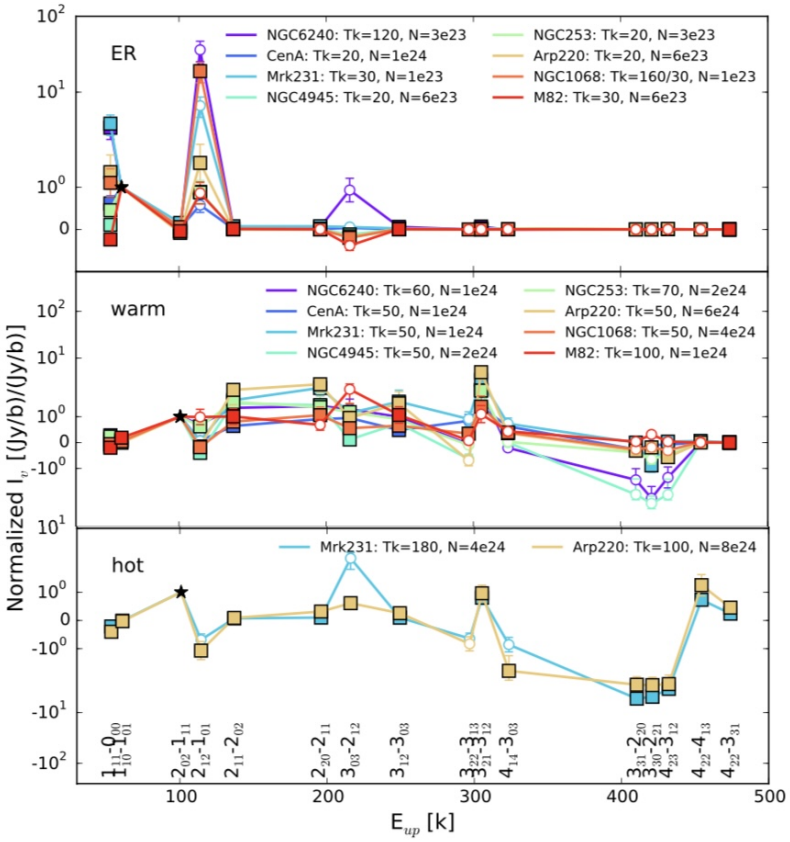

Figure 5.6: Water SLEDs for different ISM regions. From top to bottom: the cold extended region, the warm region, and the hot region. Observed transitions have been normalized to the H2O ($2_{02} - 1_{11}$) line, designated by the black stars in each panel. Adapted from Liu et al. (2017).

(such as the H_2O ($4_{22} - 4_{13}$) line) required more intense excitation sources (i.e., were not found to be collisionally excited) such as XDRs, cosmic rays, or intense turbulence or feedback.

Observations of these lines, in combination with radiative transfer modelling codes, can provide indications of the excitation sources within a galaxy required to produce such line intensities. One such example of this is the local ULIRG Mrk231 which has been detected in a wide variety of H_2O transitions. A thorough analysis of the water SLED and subsequent SED decomposition by González-Alfonso et al. (2010) suggested that PDRs are insufficient to account for the observed H_2O flux. Alternative explanations are extreme outflows/turbulence and cosmic rays, or XDRs.

Yang et al. (2016) studied 11 hyperluminous infrared galaxies (Hy-ULIRGS) and ULIRGS at $z \sim 2 - 4$ and found that water emission was strongly correlated with $L_{\rm IR}$ in their sample with the relation $L_{\rm H_2O} \propto \gamma \times L_{\rm IR}^{1.1-1.2}$ where γ is a coefficent that changes based on water transition. This correlation is thought to originate due to the effect of infrared pumping of the water lines. Infrared pumping is a process by which water transitions at lower frequencies 'pump' higher frequency water lines, in effect synthetically boosting the intensities of certain transitions.

Water lines also provide an additional means of determining the SFR of a given galaxy using the the relation from Yang et al. (2016) and Kennicutt & Evans (2012) (e.g., Jarugula et al. 2021):

$$\mathrm{SFR}[\mathrm{M}_\odot/\mathrm{yr}] \sim 1.47 \times 10^{-10} \times \mathrm{L}_{\mathrm{IR}}^{1.1-1.2}[\mathrm{L}_\odot]. \tag{5.8}$$

This relation is particularly interesting as star-formation is thought to heavily affect the specific water lines which can pump other transitions. Water lines, especially in combination with other ISM tracers, may present the new frontier of ISM-diagnostic tools in the high-redshift universe. These lines provide the unique possibility of finally beginning to disentangle the affect of star-formation versus that of the SMBH on the ISM of high-redshift galaxies.

5.3.3 Dust

General reference: Galliano (2022)

Intergalactic dust is a key ingredient in the ISM in spite of the fact that it makes up only about $\sim 1\%$ of a given galaxy's mass. Dust is made up of very small grains of matter with very complex morphologies on the order of $0.3\,\mathrm{nm} - 0.3\,\mu\mathrm{m}$ comprised typically of C, O, M, Si, S, F, or combinations thereof (e.g., Draine 2011). Dust grains are thought to play a number of significant roles in galaxy evolution.

Primarily, the surface of dust grains and the grains themselves can act as catalysts for chemical reactions. Namely, reactions that create H_2 molecules which are the most abundant molecules in the universe (e.g., Gould & Salpeter 1963; Bron et al. 2014) and hence the main constituent of the ISM (e.g., Hirashita & Ferrara 2002). Dust grains are a crucial component of star-formation (e.g., Li & Greenberg 2002) and are primarily responsible for gas heating within PDRs (e.g., Draine 1978; Kimura 2016).

Although dust grains are immensely important in galaxy evolution, their presence contributes significantly to difficulties in directly observing star-formation in galaxies. Grains absorb the UV rays from stars and re-emit their light at longer wavelengths, reprocessing up to $\sim 25\%$ of a galaxy's stellar light into the infrared regime (e.g., Calzetti 2001; Bianchi et al. 2018). The obvious implication of this fact is that studies of a galaxy's dust properties yield information not only about the dust (such as dust mass, temperature, etc.,) but also about the stellar population of the galaxy.

The effect of dust obscuration of a galaxy is constrained through analysis of its SED. The SED can be divided depending on the source of the emission, as shown in Figure 5.7. At shorter wavelengths unobscured stellar emission dominates the flux while at longer wavelengths dust re-emission of UV light is clearly the prevailing source of radiation. The dust-dominated region of the SED can be further partitioned into the Rayleigh-Jeans tail right of the peak of the dust emission and the Wien side to the left. The Rayleigh-Jeans tail is generally associated with colder dust whereas the Wien side is associated with warm dust. Dust has been observed in galaxies as distant as $z \sim 7$ (e.g., Watson et al. 2015; Knudsen et al. 2017; Hashimoto et al. 2019).

The star-formation rate of a galaxy can be inferred from a galaxy's SED using the above principles. Namely this is done by estimating the contribution of

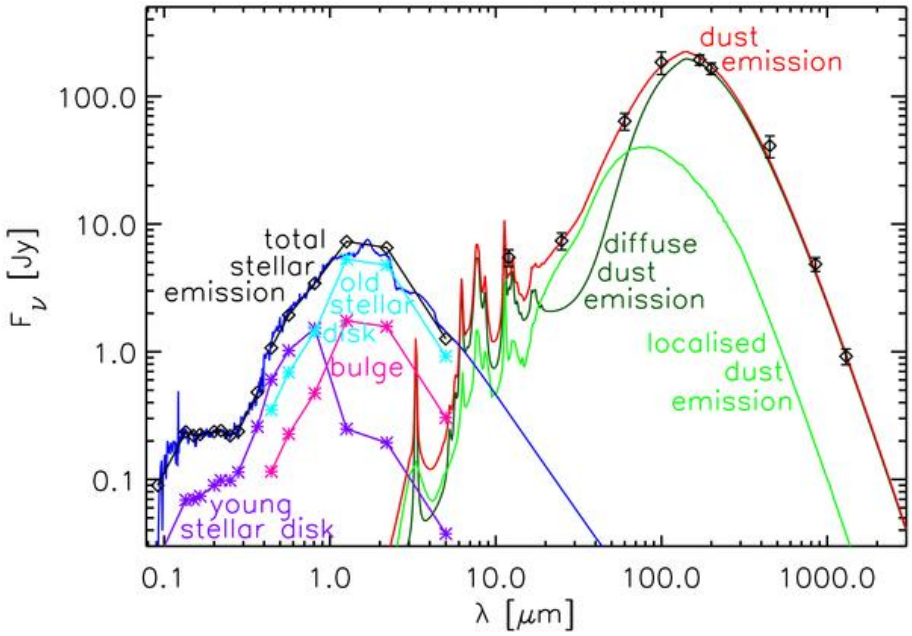

Figure 5.7: Best fit SED models for NGC 891 showing the different components including different dust components. Figure from Popescu et al. (2011).

the stellar population to the dust-dominated regions of the SED as SFR $[M_\odot yr^{-1}] \sim 1.47 \times 10^{-10}\,[L_\odot]$ (Kennicutt & Evans 2012).

5.3.4 Galaxy gas content

The categorization of the gas content of a galaxy can be used to ascribe meaning to its evolutionary point. There exist a number of methods for identifying the molecular gas content of high-redshift galaxies. These include using the CO(1-0) line and a conversion factor to obtain a H_2 gas mass, higher-J CO lines, fitting of the dust SED in the far-infrared regime, single band continuum measurements, and observations of the [C I] fine structure lines. These methods are summarized in-depth in Hodge & da Cunha (2020).

By studying the gas content of a galaxy, constraints can be placed on the galaxy's gas mass and star-formation rate efficiency (also known as the depletion time). The star-formation rate efficiency can be described as the length of time for which a galaxy has the capability to form stars, or $t_{\rm dep} = M_{\rm gas}/{\rm SFR}$. This is an important ratio as it allows for a more accurate comparison to be made about the physical meaning of the gas content rather than a simplistic comparison between numbers. Current evidence points to a decrease in $t_{\rm dep}$ with redshift, but the exact rate of this decrease is contentious (e.g., Scoville et al. 2017; Tacconi et al. 2018; Liu et al. 2019).

CHAPTER 6

THE QUASAR BRI0952-0115

As the previous chapter of this licentiate thesis have illustrated, understanding the role of the AGN and that of star formation in galaxy evolution is extremely important. In order to accomplish this it is necessary to determine the physical properties and the state of the ISM in quasar-host galaxies. One means of determining the interplay between the AGN and constituent star formation is by observing molecular and atomic emission lines from the galaxy. The energy released from both star formation and the central quasar heat the ISM, and by observing lines with a broad range of excitation temperatures and critical densities it is possible to begin to distinguish between the heating sources operating within a galaxy.

The appended paper to this thesis focuses on the two $z = 4-5$ starbursting galaxies AzTEC-3 and BRI0952−0115 (hereafter BRI0952). AzTEC-3 has been the intense focus of a number of previous studies (e.g., Riechers et al. 2010; Capak et al. 2011; Riechers et al. 2014; Guaita et al. 2022), however BRI0952 has only been modestly studied in the past (e.g., Maiolino et al. 2009; Gallerani et al. 2012). This chapter focuses specifically on BRI0952 and presents results from a project in progress for which a publication is in preparation (Kade et al. in prep.).

BRI0952 is a bright, lensed quasar at $z = 4.432$ with a previously estimated gas mass of $M_{\rm H_2} \sim (2-3) \times 10^9 {\rm M}_\odot$ (Guilloteau et al. 1999) and a star-formation rate previously estimated at $\sim 270 {\rm M}_\odot {\rm yr}^{-1}$ (Gallerani et al. 2012). BRI0952 is lensed by a line of sight galaxy at $z = 0.632$ (Eigenbrod et al. 2007) with previous estimates placing the magnification factor $\mu \sim 6.7$ (Gallerani et al. 2012). The lensing has produced a double-image system referred to as the north and south images (Img-N & Img-S) of the quasar. This galaxy was strongly detected in [C II] emission by Maiolino et al. (2009) and Gallerani et al. (2012). Summarized below are the results of a re-analysis of ALMA archival and new ALMA band 7 observations of BRI0952.

6.1 Observations

This project makes use of ALMA archival bands 3, 4, and 6 data and ALMA band 7 data originally obtained for use in a project searching for magnetic field signatures in the early universe. These are summarized in the sections below.

6.1.1 ALMA archival data

Calibration of the data were performed according to the ALMA pipeline calibration scripts using CASA 5.4.0. (CASA 2). This included calibration of the phase, bandpass, flux, and gain. The quality of the pipeline results were checked and found to be acceptable. Imaging of the source was done using CASA's TCLEAN algorithm. All sources were masked during the cleaning process.

An initial emission line search was performed on the 'dirty' images in order to identify line free channels for continuum subtraction. Subsequent continuum subtraction was done using a polynomial fit of 1. The continuum subtracted visibilities were then imaged using natural weighting. The band 3 archival data were of much higher resolution and thus were tapered to approximately match the resolutions of the band 7 data. The channel width is the same for all the observation sets, 15.6 GHz. Beam sizes, spectral window central frequencies, and final image rms' are shown in Table 6.1.

6.1.2 ALMA band 7 observations

Calibration and continuum subtraction of the data were performed in the manner described above for the archival data. The continuum subtracted visibilities were initially imaged using Briggs weighting with a robust factor of 0.5. However, for further analysis using this data to search for companion galaxies and for use in lensing modelling, the spectral window containing [C II] emission was re-imaged with a robust factor of 0.0. The channel width of the spectral window containing the [C II] line is 15.6 GHz. The channel width of the spectral windows containing the OH and OH^+ line are 31.2 GHz. Beam sizes, spectral window central frequencies, and final image rms' are shown in Table 6.1.

6.2 Results

The ALMA band 7 results yielded detections of [C II] ($^2P_{3/2} \rightarrow^2 P_{1/2}$) emission towards both images of the lensed quasar. We term these images as 'Img-N' and 'Img-S'. In addition, we detect a companion galaxy to the southwest of the quasar (Gal-SW) and tentatively detect a companion to the north of the quasar (Gal-N). Line parameters for the quasar are in Table 6.2, moment-0 maps in Figure 6.2, and spectra are shown in Figure 6.3. The [C II] emission results are utilized mainly in Paper I, however, asymmetries in the [C II] line profile prompted the creation of an updated lensing model, as described below. Additional line detections from the band 7 observations are discussed below.

Band	Date [yy mm dd]	N_{ant}	$\nu_{spw,central}$ [GHz]	Beam [" x "]	RMS [mJy/bm]
$3_{CO(5-4)}$	17 12 04	47	105.0	$[0.56 \times 0.41]$	0.25
$4_{[CI]\&CO(7-6)}$	16 02 04	42	147.5	$[1.44 \times 1.04]$	0.35
$4_{H_2O(2_{11}-2_{02})}$	16 02 04	42	139.3	$[1.55 \times 1.12]$	0.51
$6_{CO(12-11)}$	16 01 06	45	255.9	$[1.50 \times 0.93]$	0.51
$7_{[CII]}$	19 04 06	41	348.9	$[0.44 \times 0.35]$	0.56
$7_{[OH]}$	19 04 06	41	339.0	$[0.55 \times 0.45]$	0.13
$7_{[OH^+]}$	19 04 06	41	347.1	$[0.54 \pm 0.43]$	0.13

Table 6.1: ALMA data synthesized beams, antenna count, spectral window frequency, sythnesized beam size, and final image RMS. Each spectral window with a line detection is shown with the emission line detected. The band 3 archival data was of significantly higher resolution and was tapered to a beam comparable to the band 7 data.

6.2.1 Lensing model

The [C II] emission from the quasar exhibited wing-like structures, emblematic of a partial Einstein ring. This was cause for a new lensing model to be constructed as these structures were not present in previous imaging of the source, and therefore not taken into account in previous lensing models. This model was constructed using Visilens, a program designed specifically to model observations of gravitationally lensed sources at radio and mm wavelengths (Spilker et al. 2016). Visilens reduces bias in magnification factor calculations by directly modelling the interferometric *uv*-data rather than using images produced from algorithms such as CASA's tclean. The lens was modelled as a single isothermal ellipsoid (e.g., Kormann 1994) and the lens position was optimized on the continuum data before applying the configuration to the [C II] line data. Upon optimization, the output lens parameters were used to calculate the magnification factor of the [C II] line emission in 5 bins across the line (see Appendix Figure A.1 in Paper I). This was done due to apparent stronger lensing in the red part of the line emission. An average of these magnification factors was then taken and used as the magnification factor for the galaxy, $\mu = 4.0 \pm 1.3$ (Kade et al. submitted; Paper I).

6.2.2 Line detections

A number of additional lines were detected in the ALMA archival data and in the remaining spectral windows of the band 7 observations. These detections include CO(5-4), CO(7-6), CO(12-11), [C I] (2-1), an quadruplet of hyperfine OH^+ ($1_2 - 1_1$) transitions, an OH doublet in which each line was a quadruplet of hyperfine transitions, and H_2O ($2_{11} - 2_{02}$). The CO lines were fit with two-Gaussian fit to the line to account for asymmetries in the line profile, see Figure 6.3. All other emission lines, with the exception of the OH doublet, were fit with a single Gaussian. The OH doublet was fit using two Gaussian profiles. The H_2O ($2_{11} - 2_{02}$) spectrum was binned by a factor 2 to increase data quality. Line parameters are shown in Table 6.2, moment-0 maps in Figure 6.2, and spectra in Figure 6.3.

Table 6.2: Line parameters for emission lines detected in BRI0952. The line luminosities are corrected for lensing using the lensing factor found in Paper I of $\mu = 4$ (Kade et al. Submitted).

Line	ν_{rest} [GHz]	ν_{obs} [GHz]	$I_{\rm line}$ [Jy km s^{-1}]	FWHM [km s^{-1}]	$L_{\rm line}$ 10^8 [$L_\odot$]
CO(5-4)	576.26	106.09	0.91 ± 0.14	115 ± 46	0.4 ± 0.1
				206 ± 27	
CO(7-6)	806.65	148.55	1.5 ± 0.13	93 ± 37	1.0 ± 0.1
				246 ± 16	
CO(12-11)	1382.0	254.4	1.74 ± 0.14	23 ± 44	2.0 ± 0.2
				259 ± 14	
[CI]	809.34	149.05	0.10 ± 0.08	239 ± 146	0.07 ± 0.06
[CII]	1900.54	349.77	16.6 ± 1.6	190 ± 5	26 ± 0.2
				400 ± 19	
H_2O ($2_{11} - 2_{02}$)	752.03	138.49	0.09 ± 0.03	235 ± 59	0.05 ± 0.02
OH	1834.75	337.77	2.3 ± 0.20	287 ± 17	3.4 ± 0.3
	1837.75	338.30	2.3 ± 0.20	286 ± 16	3.5 ± 0.3
OH^+	1892.23	348.4	0.12 ± 0.01	248 ± 23	0.18 ± 0.02

The two companion galaxies (Gal-SW and Gal-N) were located sufficiently close to the quasar as to be blended with Img-N and Img-S for observations with larger beams than that of the band 7 data. However, their very low luminosities in comparison to the quasar meant that they were unlikely to contribute in any significant way to other emission lines. However, we do not rule out that the asymmetries in the line profiles of the CO lines are, at least in part, affected by these companions.

6.2.3 SED fitting

An IR SED fit was performed using DecompIR (Mullaney et al. 2011) following the methodology described in Stanley et al. (2018) using MIPS 24 μm, WISE bands, and ALMA bands 3, 4, 6, and 7 continuum data. The SED of the quasar was best fit using a combination of both AGN and star-formation templates.

The result of this was a $L_{\rm IR}$ (integrated from 8-1000 μm) that could be decomposed into the contribution from the AGN - $L_{\rm IR_{AGN}} = (2.23 \pm 0.72) \times 10^{14} L_\odot$ - and that from star-formation - $L_{\rm IR_{SF}} = (7.66 \pm 2.49) \times 10^{12} L_\odot$. Using the $L_{\rm IR_{SF}}$, a SFR for the quasar was found of $\sim 770 {\rm M}_\odot {\rm yr}^{-1}$. The SED of BRI0952 is shown in Figure 6.1.

6.3 Excitation

The CO SLED of BRI0952, normalized to the CO(5-4) transition and shown in Figure 6.4, demonstrates an increase in intensity with increasing J. As noted in Chapter 5.3.2.1, this indicates that there are likely extreme radiation sources operating within BRI0952. There are two possible origins of this excitation; the first being that the AGN is heavily affecting the ISM conditions within the galaxy and

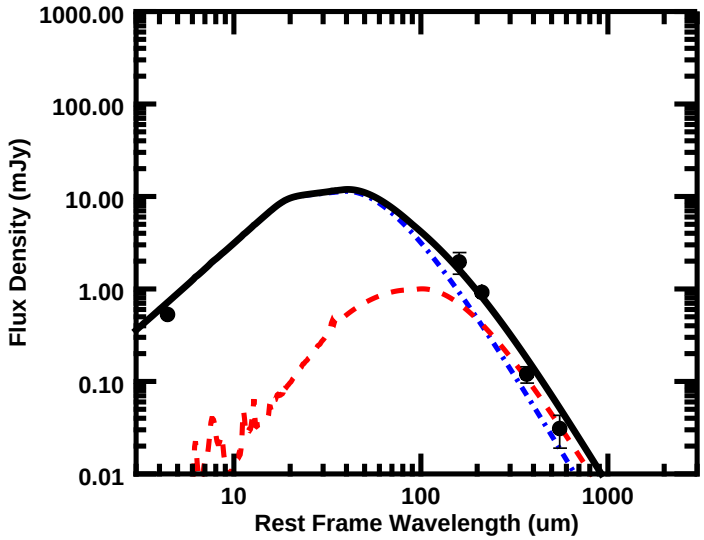

Figure 6.1: SED of BRI0952. The black line shows the best fit to the data. The blue line shows the AGN contribution to the SED fit and the red line shows the contribution from star formation. Figure from Kade et al. (in prep).

producing high-J CO transitions and the second is that that the effect of the AGN is limited to the nuclear region of the quasar and the main contributor is intense ongoing star-formation. However, the detection of the high-J CO transitions in combination with the SED fit suggest that the AGN plays a large role in the ISM conditions of BRI0952.

The $H_2O(2_{11} - 2_{10})$ line exhibits a similar line profile to the CO(7-6) and CO(5-4) lines, consistent with the trend observed in previous studies of similar line profiles of H_2O and higher-J CO lines (e.g., van der Werf et al. 2011; Stanley et al. 2021). An analysis of the $H_2O(2_{11} - 2_{10})$ line shows that the line luminosity follows the trend found by Yang et al. (2016) when using the $L_{\mathrm{IR_{SF}}}$, suggesting that IR pumping could be affecting the water line fluxes in this source, see Figure 6.5.

In combination, these atomic and molecular tracers mean that the ISM of BRI0952 is one of the most-extensive studied at high-redshift. Due to the unclear nature of the affect of the AGN on the heating processes of the ISM, an in-depth analysis of the observed lines and radiative transfer modelling will be performed with the aim of providing insight and differentiation to the question of the origin of the heating processes.

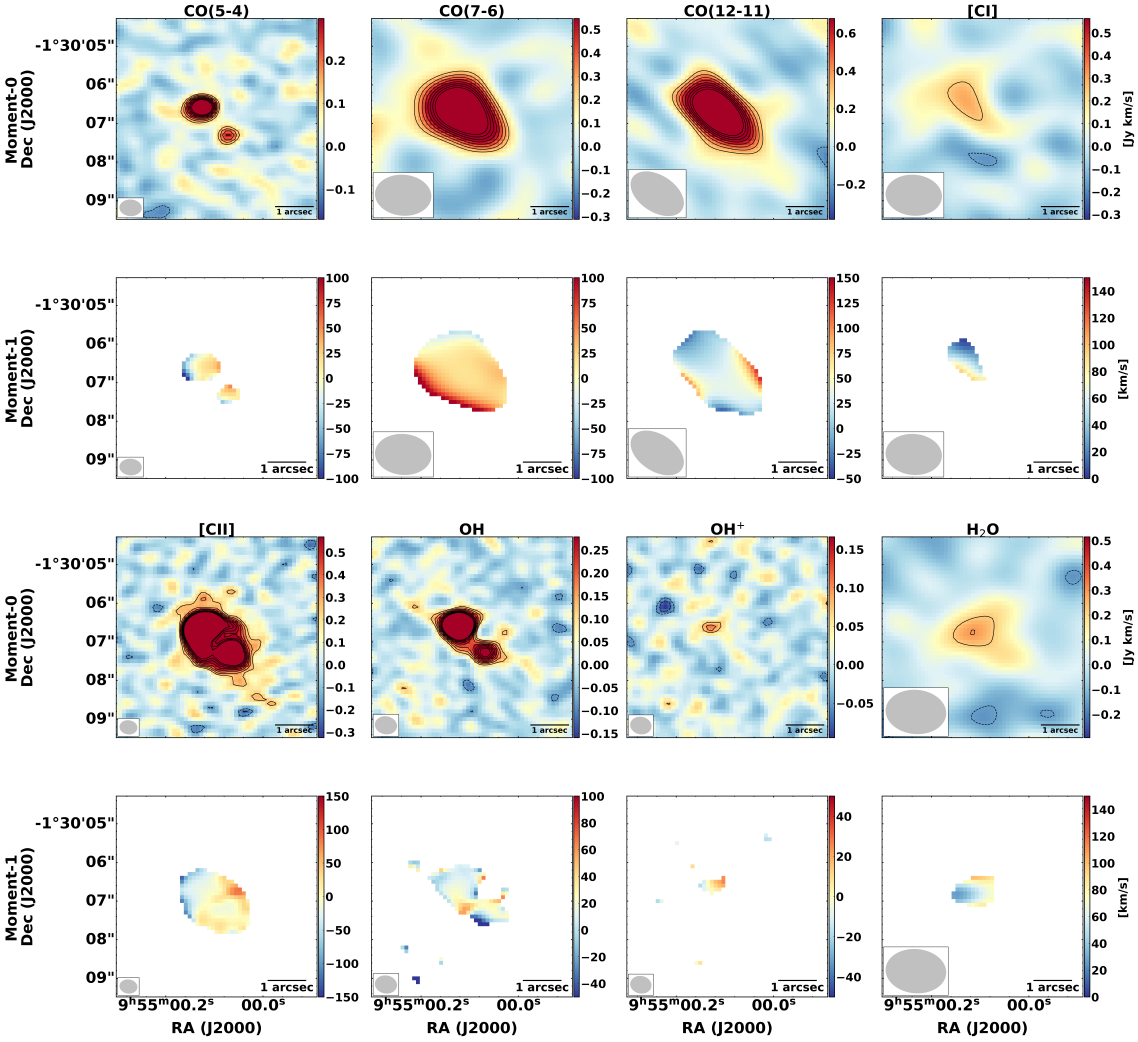

Figure 6.2: Moment-0 and moment-1 maps for the lines detected in BRI0952. The synthesized beam is shown in the bottom left corner of the image. The contours are shown at $-3, -2, 3, 4, 5, 6, 7, 8, 9, 10\sigma$ levels. Figure from Kade et al. (in prep).

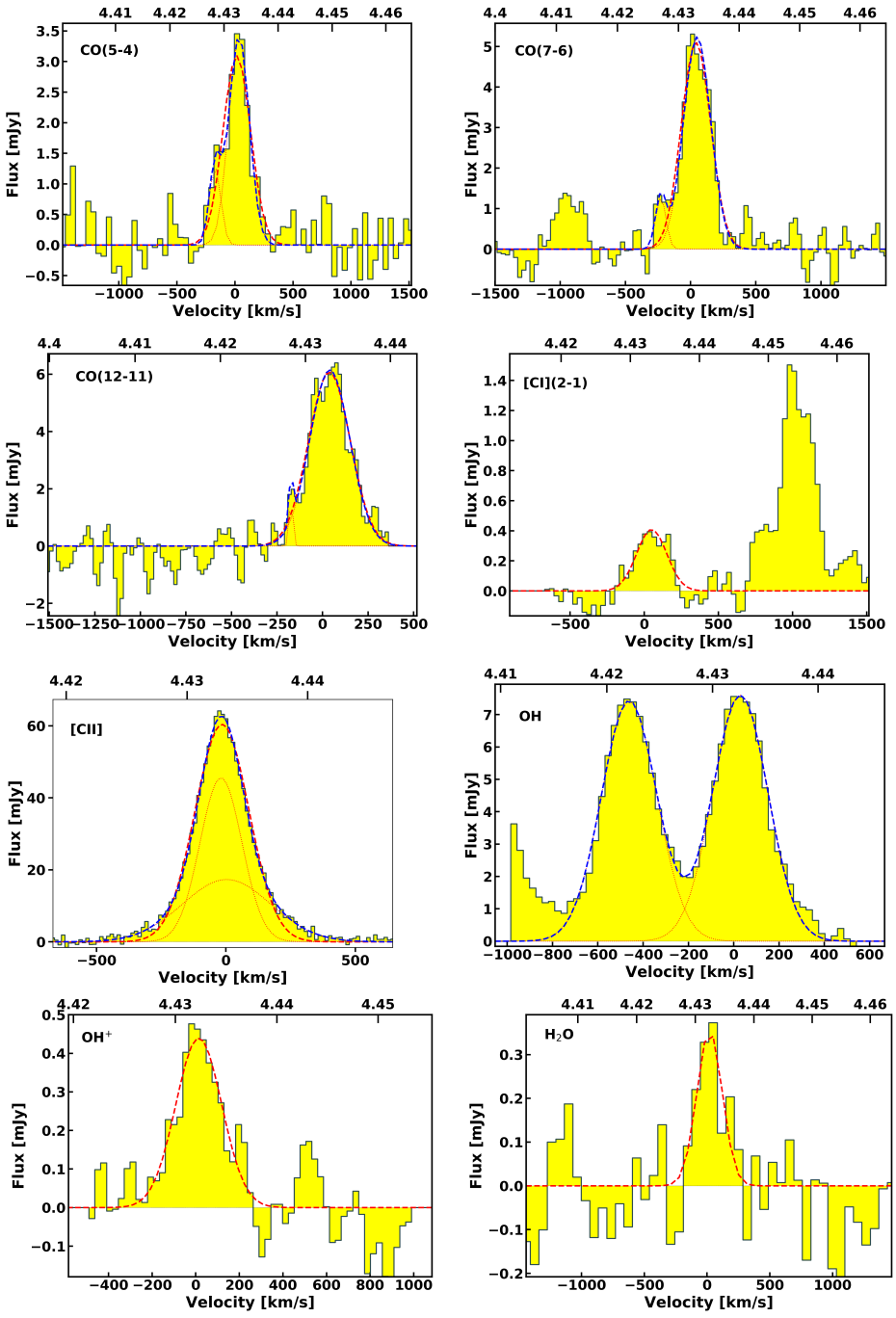

Figure 6.3: Spectra of emission lines detected in BRI0952. The red represent single Gaussian fits and the blue double Gaussian fits. Figure from Kade et al. (in prep.).

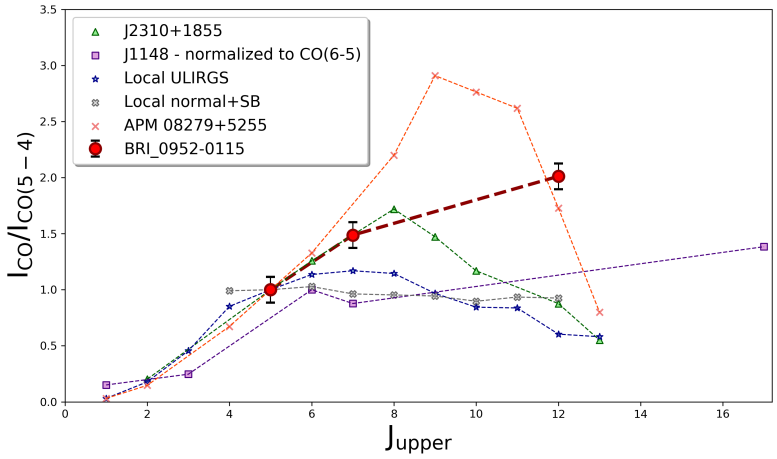

Figure 6.4: CO SLED for BRI0952 and other local and high-redshift analogues, normalized to CO(5-4) (with the exception of J1148 which was normalized to CO(6-5)). Figure from Kade et al. (in prep).

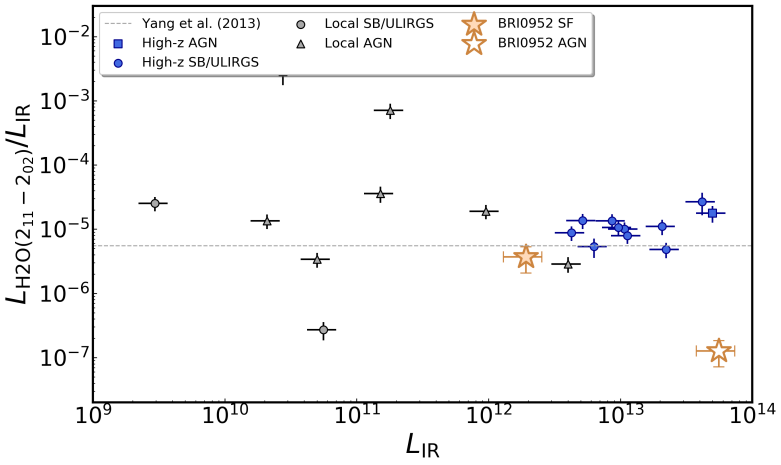

Figure 6.5: $L_{\mathrm{H_2O}}/L_{IR}$ verses L_{IR} for BRI0952 and a sample of other local and high-redshift galaxies. Two stars are shown for BRI0952, the empty star designates the $L_{\mathrm{IR_{AGN}}}$ while the filled star shows the $L_{\mathrm{IR_{SF}}}$. The ratio for BRI0952 is similar to other high-redshift AGN and starburst galaxies when using the $L_{\mathrm{IR_{SF}}}$. Figure from Kade et al. (in prep).

CHAPTER 7

RESULTS OF APPENDED PAPER

7.1 Introduction to Paper I

Paper I aims to place the SMG AzTEC-3 ($z = 5.3$, introduced in Chapter 3) and quasar BRI0952 ($z = 4.432$, discussed in-depth in Chapter 6) into the over-arching context of massive galaxy evolution in the high-redshift universe. Previous studies using ALMA observations of similar sources have begun to yield detections of smaller, fainter companion galaxies to massive high-redshift galaxies (e.g., Carilli et al. 2013; Riechers et al. 2014; Decarli et al. 2017; Díaz-Santos et al. 2018; Neeleman et al. 2019; Venemans et al. 2020). Bearing this in mind, an analysis of the environment of both AzTEC-3 and BRI0952 was performed using [C II] line emission from high-resolution band 7 ALMA observations. These observations were originally intended to search for magnetic field signatures in either of these sources, seeking what would have been the first detection of magnetic fields at high-redshift. Thus, the integration time for the sources was quite high, a necessary condition for attempts to detect the desired companion galaxies. In addition to this, [C II] line emission data was used to characterize the environment, magnetic fields, and outflow signatures from and around BRI0952 and AzTEC-3.

7.2 Results of Paper I

Paper I focused on three different aspects of BRI0952 and AzTEC-3, each provided by the [C II] observations. These aspects were the environment in which these galaxies exist, outflow signatures in both of their [C II] line profiles, and a search for indications of magnetic fields in both galaxies. The main results are summarized below.

Three companion galaxies were detected in close proximity to AzTEC-3: Gal-S, Gal-SW, and LBG-3. Each of these companions is visible in *HST* imaging of the protocluster. LBG-3 was previously noted as a non-detection in [C II] with a 3σ upper limit (Riechers et al. 2014), and further investigated through Lyman-α by Guaita et al. (2022). A bridge of [C II] emission seems to connect Gal-S and

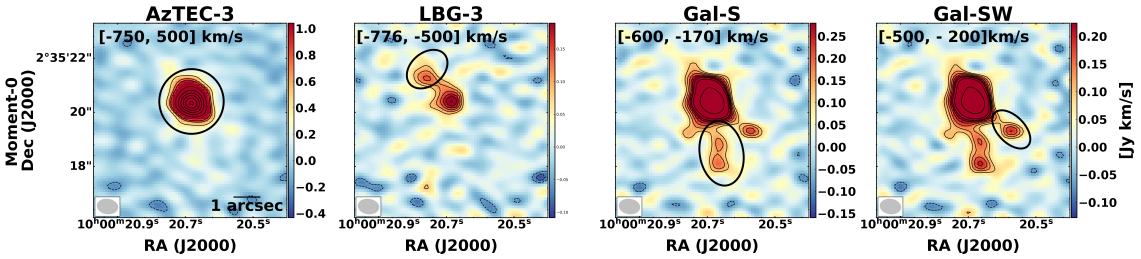

Figure 7.1: [C II] moment-0 map of the AzTEC-3 system for AzTEC-3, LBG-3, Gal-S, and Gal-SW. The top left corner of each image shows the velocity range from which the spectra was extracted for each source. The black circle for AzTEC-3 and ellipses for the remaining sources represent the regions from which the spectra of each was extracted. The contours are shown at $-3, -2, 10, 20, 30, 40, 50, 60\sigma$ levels for AzTEC-3 and $-3, -2, 3, 4, 5, 6, 7\sigma$ levels for the companions. Figure from Kade et al. Submitted.

AzTEC-3, in a similar manner to the gas-bridge structure detected in the Hot DOG W2246-0526 (Díaz-Santos et al. 2018). An additional gas feature, possibly tidal in nature, between LBG-3 and AzTEC-3 was tentatively detected. This feature was also tentatively noted in Riechers et al. (2014) and was the subject of intense investigation in Guaita et al. (2022). The companion galaxies to AzTEC-3 exhibit [C II] emission at $\sim 3\%$ that of the SMG. The moment-0 maps for the AzTEC-3 system are shown in Figure 7.1.

In the case of BRI0952, the detection of a companion galaxy to the south-west of the quasar (Gal-SW) confirmed its tentative first detection by Gallerani et al. (2012). In addition, another source of emission is tentatively detected to the north of the quasar and is assumed to be a companion galaxy. These galaxies are not detected in *HST* imaging and are located at $0.7''$ and $2.3''$, respectively, from the Img-N of the quasar. They exhibit [C II] emission at about 4% that of BRI0952.

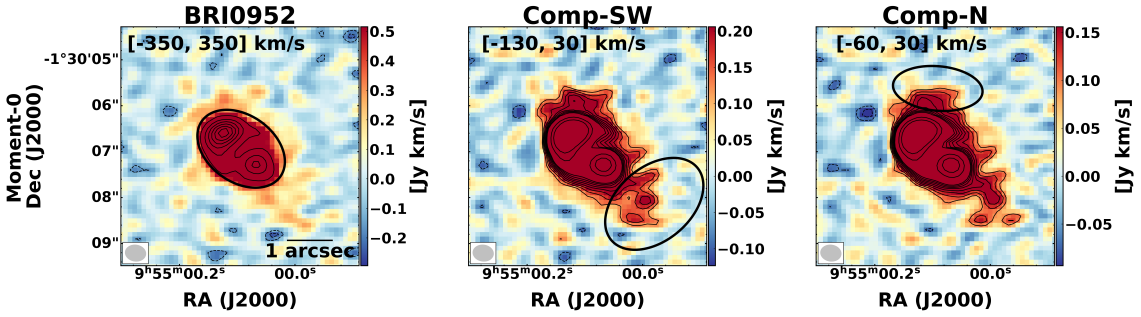

Figure 7.2: [C II] moment-0 map of the BRI0952 system for BRI0952, Comp-SW, and Comp-N. The top left corner of each image shows the velocity range from which the spectra was extracted for each source. The black circle ellipses represent the regions from which the spectra of each was extracted. The contours are shown at $-3, -2, 10, 20, 30, 40, 50, 60\sigma$ levels for BRI0952 and $-3, -2, 3, 4, 5, 6, 7\sigma$ levels for the companions. Figure from Kade et al. Submitted.

The [C II] spectra of both galaxies exhibit high-velocity wings. This fea-

ture is generally interpreted as gas flows with high velocity and typically associated with outflows. For the purposes of Paper I, these wings were assumed to be a signature of outflows. However, we note the possibility that the wings are caused by a contamination of the [C II] line profile by the companion galaxies.

Under the assumption that these wings are indeed outflow signatures, we calculate the mass outflow rate using a spherical geometry following the procedure described in Maiolino et al. (2012), Cicone et al. (2015), and Stanley et al. (2019). This results in a mass outflow rate of $\dot{M}_{\rm out} = 258 \pm 29 {\rm M}_{\odot}{\rm yr}^{-1}$ for AzTEC-3 and $\dot{M}_{\rm out} = 97 \pm 18 {\rm M}_{\odot}{\rm yr}^{-1}$ for BRI0952. In the case of BRI0952, this value is lower than those found for quasar-driven outflows such as Feruglio et al. (2010); Sturm et al. (2011); Cano-Díaz et al. (2012); Maiolino et al. (2012); Cicone et al. (2015); Feruglio et al. (2015), but in good agreement with results from stacking approaches such as Gallerani et al. (2018); Stanley et al. (2019); Ginolfi et al. (2020).

An SED fit was performed for both galaxies, and thus a SFR calculated. Both galaxies have high SFRs (BRI0952: $\sim 770 {\rm M}_{\odot}{\rm yr}^{-1}$ and AzTEC-3: $7340 {\rm M}_{\odot}{\rm yr}^{-1}$). We fit simple modified black body approximations to find an approximate $L_{\rm IR}$ for the companion sources for both. Additionally, we investigate the [C II] deficit and find that in AzTEC-3 and BRI0952 this deficit is similar to other high-redshift galaxies but that the companions compare better to local galaxies (i.e., exhibit a smaller deficit).

We use a virial mass estimator using the FWHM of the [C II] line following the procedure described in Riechers et al. (2014) to estimate the mass of the respective companion galaxies of both AzTEC-3 and BRI0952. We find that they have masses of $\leq 4\times$ for that of AzTEC-3 and $\sim 1.5-2\times$ for that of BRI0952. We stress the caveat that the masses of the companions of BRI0952 are likely overestimated as we do not correct for lensing when calculating their mass. In the case of AzTEC-3, the observation of features linked to interactions suggest that these companions may be in the process of merging with the SMG, and their masses classify them as minor mergers.

Based on theoretical predictions that [C II] may trace magnetic fields (e.g., Yan & Lazarian 2012; Zhang et al. 2015; Zhang & Yan 2018), the observations were designed to constrain the magnetic fields of both AzTEC-3 and BRI0952. However, the full polarization data yielded a non-detection. Limits on the B-field are given in Table 2 in Paper I.

The results of this study demonstrate the striking ability of ALMA to detect and (at least partially) resolve very faint companion galaxies in the high-redshift universe. The extreme star-formation rates of these galaxies indicate their need for gas obtainment and thus raise the question of the role of their faint companions in their evolution. Future deep high-resolution ALMA observations of similar galaxies in the high-redshift universe will uncover the role and ubiquity of these faint companions in the years to come.

My contribution to Paper I included performing a full analysis of the data including imaging, continuum subtraction, source detection, spectral and continuum analysis, SED fitting for AzTEC-3, star-formation rate calculations, mass-outflow rate calculations, and dynamical mass calculations. The observations were reduced and calibrated by ALMA and the regional center ARC node. I was not involved

in the polarization results and the magnetic field analysis, this was performed by a co-author. Additionally, SED fitting of BRI0952 was performed by a co-author. I wrote the manuscript text with the exception of subjects relating to magnetic fields.

CHAPTER 8

SUMMARY & OUTLOOK

The way in which massive galaxies evolve at high-redshifts is still an open question with significant progress left to be made. Evidence from simulations of the early universe suggest that feedback effects and the environment in which massive galaxies grow play a key role in their development. These processes are thought to govern their star-formation, morphology, and even regulate the growth of the central SMBH. Only by studying these key factors can a clear determination be made about their capacity to influence the evolution of these galaxies.

Understanding the effect of environment on the evolution of massive galaxies in the early universe is an arduous task to undertake. Detecting even massive companion galaxies to massive galaxies is a challenge, with faint companions only beginning to be discovered in the past decade. Indeed, a number of studies have found evidence for tidal structures, bridges, or streams of gas between the detected smaller and fainter companions to their massive counterparts (e.g., Díaz-Santos et al. 2018; Guaita et al. 2022). Through studying the environment of different classes of high-redshift galaxies (e.g., quasars, SMGs), the observed differences in these classifications can begin to place them into an evolutionary context.

In the local universe, feedback effects can be observed with relative ease, at least compared to the high-redshift universe where distance compounds with technical limitations. Certain studies of high-redshift quasars have claimed detection of massive outflows through high-velocity [C II] spectral wings, only to be disproven with the acquirement of better data (e.g., Maiolino et al. 2012; Cicone et al. 2015; Meyer et al. 2022b). In contrast, other studies using more standard outflow tracers, such as OH, detected clear outflow signatures in $z > 4$ galaxies (e.g., Spilker et al. 2020; Butler et al. 2021). A wide range of mass-outflow rates have been suggested from these studies. A main concern with all studies of feedback in the high-redshift universe is the origin and nature of the outflow and the true effect of the outflow on the evolution of the galaxy (e.g., Spilker et al. 2020; Scholtz et al. 2020).

The work of this licentiate thesis has been focused, thus far, on the environment of the two massive galaxies BRI0952-0115 and AzTEC-3 in the early universe. These two galaxies represent prime candidates for ISM and environment studies. The focus of Paper I was to investigate the environment and the effect

of faint companion galaxies. The results of Paper I, summarized in the previous chapter, demonstrate both the observational capability of ALMA and the distinct need for additional observations of this kind to determine the true impact of the environment.

Concrete future work of this thesis will comprise of investigations of the ISM of the quasar BRI0952 using multi-band ALMA observations, for which tentative first results were described in Chapter 6. The main goal of this work will be to attempt to disentangle the ways in which the AGN affects the ISM of the galaxy, in comparison to the effects of star formation. In addition, a source-plane reconstruction of BRI0952 will be performed to better constrain both the effects of lensing on the line profiles of emission lines and to better understand the nature of the outflow signatures.

In less concrete terms, a more detailed investigation of the effect of the faint companion sources on AzTEC-3 would be compelling. Observations of shock tracers such as methanol or SiO could provide clues as to whether a merger is in process in this system. Furthermore, observations of a number of water transitions with excitation conditions ranging from collisional to radiative could also assist in determining the conditions of AzTEC-3. This would also be highly useful for BRI0952, especially in distinguishing the effect of the AGN from that of star-formation. Proposals for observations of this sort will be submitted for the upcoming ALMA Cycle 9 call for proposals.

Observations in the coming years will continue to provide clues to the processes governing the evolution of massive galaxies in the high-redshift universe. The means by which these galaxies sustain intense star-formation rates will become increasingly clear with additional deep high-resolution observations. Knowledge of the role of the AGN and feedback effects from the AGN will increase with the expanding toolbox of lines used to trace these processes. The next generation of powerful telescopes (e.g., SKA, Large Synoptic Survey Telescope (LSST), Extremely Large Telescope (ELT), *James Webb Space Telescope (JWST)*, etc.) will play a decisive role in these discoveries, along with the already operational ALMA telescope. The evolution of high-redshift massive galaxies shall not remain enshrouded in mystery for long.

BIBLIOGRAPHY

Aalto, S., Falstad, N., Muller, S., et al. 2020, A&A, 640, A104

Aalto, S., Garcia-Burillo, S., Muller, S., et al. 2012, A&A, 537, A44

Alatalo, K., Blitz, L., Young, L. M., et al. 2011, ApJ, 735, 88

Andreani, P., Retana-Montenegro, E., Zhang, Z.-Y., et al. 2018a, A&A, 615, A142

Andreani, P., Retana-Montenegro, E., Zhang, Z.-Y., et al. 2018b, A&A, 615, A142

Antonucci, R. 1993, ARA&A, 31, 473

Assef, R. J., Eisenhardt, P. R. M., Stern, D., et al. 2015, ApJ, 804, 27

Bañados, E., Venemans, B., Walter, F., et al. 2013, ApJ, 773, 178

Barnes, J. E. & Hernquist, L. 1998, ApJ, 495, 187

Beckmann, R. S., Devriendt, J., Slyz, A., et al. 2017, MNRAS, 472, 949

Beifiori, A., Courteau, S., Corsini, E. M., & Zhu, Y. 2012, MNRAS, 419, 2497

Bennert, V. N., Treu, T., Auger, M. W., et al. 2015, ApJ, 809, 20

Bergin, E. A., Kaufman, M. J., Melnick, G. J., Snell, R. L., & Howe, J. E. 2003, ApJ, 582, 830

Bianchi, S., De Vis, P., Viaene, S., et al. 2018, A&A, 620, A112

Bischetti, M., Feruglio, C., Piconcelli, E., et al. 2021, A&A, 645, A33

Bischetti, M., Maiolino, R., Carniani, S., et al. 2019, A&A, 630, A59

Blain, A. W., Smail, I., Ivison, R. J., Kneib, J. P., & Frayer, D. T. 2002, Phys. Rep., 369, 111

Bolatto, A. D., Wolfire, M., & Leroy, A. K. 2013, ARA&A, 51, 207

Bothwell, M. S., Smail, I., Chapman, S. C., et al. 2013, MNRAS, 429, 3047

Bower, R. G., Benson, A. J., Malbon, R., et al. 2006, MNRAS, 370, 645

Brinchmann, J., Charlot, S., White, S. D. M., et al. 2004, MNRAS, 351, 1151

Bron, E., Le Bourlot, J., & Le Petit, F. 2014, A&A, 569, A100

Butler, K. M., van der Werf, P. P., Rybak, M., et al. 2021, ApJ, 919, 5

Calzetti, D. 2001, PASP, 113, 1449

Cano-Díaz, M., Maiolino, R., Marconi, A., et al. 2012, A&A, 537, L8

Capak, P. L., Riechers, D., Scoville, N. Z., et al. 2011, Nature, 470, 233

Carilli, C. L., Riechers, D., Walter, F., et al. 2013, ApJ, 763, 120

Carilli, C. L. & Walter, F. 2013, ARA&A, 51, 105

Casey, C. M., Chen, C.-C., Cowie, L. L., et al. 2013, MNRAS, 436, 1919

Casey, C. M., Narayanan, D., & Cooray, A. 2014, Phys. Rep., 541, 45

Casey, C. M., Zavala, J. A., Aravena, M., et al. 2019, ApJ, 887, 55

Cernicharo, J., Goicoechea, J. R., Daniel, F., et al. 2006, ApJ, 649, L33

Chapman, S. C., Blain, A. W., Smail, I., & Ivison, R. J. 2005, ApJ, 622, 772

Choi, E., Somerville, R. S., Ostriker, J. P., Naab, T., & Hirschmann, M. 2018, ApJ, 866, 91

Cicone, C., Maiolino, R., Gallerani, S., et al. 2015, A&A, 574, A14

Cicone, C., Maiolino, R., Sturm, E., et al. 2014, A&A, 562, A21

Cicone, C., Severgnini, P., Papadopoulos, P. P., et al. 2018, ApJ, 863, 143

Ciotti, L., Ostriker, J. P., & Proga, D. 2010, ApJ, 717, 708

Conselice, C. J. 2014, ARA&A, 52, 291

Cortijo-Ferrero, C., González Delgado, R. M., Pérez, E., et al. 2017, A&A, 606, A95

Crain, R. A., Schaye, J., Bower, R. G., et al. 2015, MNRAS, 450, 1937

Cresci, G. & Maiolino, R. 2018, Nature Astronomy, 2, 179

Croton, D. J., Springel, V., White, S. D. M., et al. 2006, MNRAS, 365, 11

Daddi, E., Dickinson, M., Morrison, G., et al. 2007, ApJ, 670, 156

Dasyra, K. M., Tacconi, L. J., Davies, R. I., et al. 2007, ApJ, 657, 102

De Looze, I., Cormier, D., Lebouteiller, V., et al. 2014, A&A, 568, A62

Decarli, R., Mignoli, M., Gilli, R., et al. 2019, A&A, 631, L10

Decarli, R., Walter, F., Neri, R., et al. 2012, ApJ, 752, 2

Decarli, R., Walter, F., Venemans, B. P., et al. 2017, Nature, 545, 457

Decarli, R., Walter, F., Venemans, B. P., et al. 2018, ApJ, 854, 97

Dekel, A., Birnboim, Y., Engel, G., et al. 2009, Nature, 457, 451

Di Matteo, T., Khandai, N., DeGraf, C., et al. 2012, ApJ, 745, L29

Di Matteo, T., Springel, V., & Hernquist, L. 2005, Nature, 433, 604

Díaz-Santos, T., Armus, L., Charmandaris, V., et al. 2013, ApJ, 774, 68

Díaz-Santos, T., Assef, R. J., Blain, A. W., et al. 2018, Science, 362, 1034

Draine, B. T. 1978, ApJS, 36, 595

Draine, B. T. 2011, ApJ, 732, 100

Dubois, Y., Pichon, C., Welker, C., et al. 2014, MNRAS, 444, 1453

Duchêne, G. & Kraus, A. 2013, ARA&A, 51, 269

Dwek, E. & Arendt, R. G. 2020, ApJ, 901, 36

Ebeling, H., Stockmann, M., Richard, J., et al. 2018, ApJ, 852, L7

Eigenbrod, A., Courbin, F., & Meylan, G. 2007, A&A, 465, 51

Eisenhardt, P. R. M., Wu, J., Tsai, C.-W., et al. 2012, ApJ, 755, 173

Elbaz, D., Daddi, E., Le Borgne, D., et al. 2007, A&A, 468, 33

Emonts, B. H. C., Lehnert, M. D., Dannerbauer, H., et al. 2018, MNRAS, 477, L60

Engel, H., Tacconi, L. J., Davies, R. I., et al. 2010, ApJ, 724, 233

Fabian, A. C. 2012, ARA&A, 50, 455

Fan, L., Han, Y., Nikutta, R., Drouart, G., & Knudsen, K. K. 2016, ApJ, 823, 107

Farrah, D., Lebouteiller, V., Spoon, H. W. W., et al. 2013, ApJ, 776, 38

Ferrarese, L. & Merritt, D. 2000, ApJ, 539, L9

Feruglio, C., Fiore, F., Carniani, S., et al. 2015, A&A, 583, A99

Feruglio, C., Maiolino, R., Piconcelli, E., et al. 2010, A&A, 518, L155

Fogasy, J., Knudsen, K. K., Drouart, G., Lagos, C. D. P., & Fan, L. 2020, MNRAS, 493, 3744

Fogasy, J., Knudsen, K. K., Lagos, C. D. P., Drouart, G., & Gonzalez-Perez, V. 2017, A&A, 597, A123

Förster Schreiber, N. M., Genzel, R., Lutz, D., & Sternberg, A. 2003a, ApJ, 599, 193

Förster Schreiber, N. M., Genzel, R., Lutz, D., & Sternberg, A. 2003b, ApJ, 599, 193

Futamase, T. 2015, International Journal of Modern Physics D, 24, 1530011

Gaibler, V., Khochfar, S., & Krause, M. 2011, MNRAS, 411, 155

Gallagher, R., Maiolino, R., Belfiore, F., et al. 2019, MNRAS, 485, 3409

Gallerani, S., Ferrara, A., Neri, R., & Maiolino, R. 2014, MNRAS, 445, 2848

Gallerani, S., Neri, R., Maiolino, R., et al. 2012, A&A, 543, A114

Gallerani, S., Pallottini, A., Feruglio, C., et al. 2018, MNRAS, 473, 1909

Galliano, F. 2022, Habilitation Thesis, 1

Gao, Y. & Solomon, P. M. 2004, ApJ, 606, 271

Gebhardt, K., Bender, R., Bower, G., et al. 2000, ApJ, 539, L13

Gerin, M. & Phillips, T. G. 2000, ApJ, 537, 644

Giavalisco, M. 2002, ARA&A, 40, 579

Ginolfi, M., Jones, G. C., Béthermin, M., et al. 2020, A&A, 633, A90

González-Alfonso, E., Fischer, J., Bruderer, S., et al. 2013, A&A, 550, A25

González-Alfonso, E., Fischer, J., Isaak, K., et al. 2010, A&A, 518, L43

Gould, R. J. & Salpeter, E. E. 1963, ApJ, 138, 393

Graciá-Carpio, J., Sturm, E., Hailey-Dunsheath, S., et al. 2011, ApJ, 728, L7

Granato, G. L., De Zotti, G., Silva, L., Bressan, A., & Danese, L. 2004, ApJ, 600, 580

Guaita, L., Aravena, M., Gurung-Lopez, S., et al. 2022, arXiv e-prints, arXiv:2202.03883

Guilloteau, S., Omont, A., Cox, P., McMahon, R. G., & Petitjean, P. 1999, A&A, 349, 363

Gültekin, K., Richstone, D. O., Gebhardt, K., et al. 2009, ApJ, 698, 198

Häring, N. & Rix, H.-W. 2004, ApJ, 604, L89

Harrison, C. M. 2017, Nature Astronomy, 1, 0165

Hashimoto, T., Inoue, A. K., Mawatari, K., et al. 2019, PASJ, 71, 71

Heckman, T. M. & Best, P. N. 2014, ARA&A, 52, 589

Hirashita, H. & Ferrara, A. 2002, MNRAS, 337, 921

Hirschmann, M., Dolag, K., Saro, A., et al. 2014, MNRAS, 442, 2304

Hodge, J. A. & da Cunha, E. 2020, Royal Society Open Science, 7, 200556

Högbom, J. A. 1974, A&AS, 15, 417

Hopkins, P. F., Hernquist, L., Cox, T. J., & Kereš, D. 2008, ApJS, 175, 356

Hopkins, P. F., Somerville, R. S., Hernquist, L., et al. 2006, ApJ, 652, 864

Husband, K., Bremer, M. N., Stanway, E. R., & Lehnert, M. D. 2015, MNRAS, 452, 2388

Jarugula, S., Vieira, J. D., Weiss, A., et al. 2021, ApJ, 921, 97

Jones, G. C., Maiolino, R., Caselli, P., & Carniani, S. 2019, A&A, 632, L7

Jones, S. F., Blain, A. W., Stern, D., et al. 2014, MNRAS, 443, 146

Katz, N., Keres, D., Dave, R., & Weinberg, D. H. 2003, in Astrophysics and Space Science Library, Vol. 281, The IGM/Galaxy Connection. The Distribution of Baryons at z=0, ed. J. L. Rosenberg & M. E. Putman, 185

Kauffmann, G. & Haehnelt, M. 2000, MNRAS, 311, 576

Kaviraj, S., Devriendt, J., Dubois, Y., et al. 2015, MNRAS, 452, 2845

Kennefick, J. D., Djorgovski, S. G., & de Carvalho, R. R. 1995, AJ, 110, 2553

Kennicutt, R. C. & Evans, N. J. 2012, ARA&A, 50, 531

Kereš, D., Katz, N., Weinberg, D. H., & Davé, R. 2005, MNRAS, 363, 2

Kimura, H. 2016, MNRAS, 459, 2751

King, A. & Pounds, K. 2015, ARA&A, 53, 115

Knudsen, K. K., Watson, D., Frayer, D., et al. 2017, MNRAS, 466, 138

Kormendy, J. & Ho, L. C. 2013, ARA&A, 51, 511

Kreckel, K., Platen, E., Aragón-Calvo, M. A., et al. 2011, AJ, 141, 4

Krips, M., Martín, S., Sakamoto, K., et al. 2016, A&A, 592, L3

Lada, C. J. & Lada, E. A. 2003, ARA&A, 41, 57

Lagache, G., Cousin, M., & Chatzikos, M. 2018, A&A, 609, A130

Lamperti, I., Harrison, C. M., Mainieri, V., et al. 2021, A&A, 654, A90

Li, A. & Greenberg, J. M. 2002, ApJ, 577, 789

Li, J., Wang, R., Riechers, D., et al. 2020, ApJ, 889, 162

Licquia, T. C. & Newman, J. A. 2015, ApJ, 806, 96

Lin, L., Patton, D. R., Koo, D. C., et al. 2008, ApJ, 681, 232

Litke, K. C., Marrone, D. P., Spilker, J. S., et al. 2019, ApJ, 870, 80

Liu, D., Schinnerer, E., Groves, B., et al. 2019, ApJ, 887, 235

Liu, L., Weiß, A., Perez-Beaupuits, J. P., et al. 2017, ApJ, 846, 5

Madau, P. & Dickinson, M. 2014, ARA&A, 52, 415

Magorrian, J., Tremaine, S., Richstone, D., et al. 1998, AJ, 115, 2285

Maiolino, R., Caselli, P., Nagao, T., et al. 2009, A&A, 500, L1

Maiolino, R., Gallerani, S., Neri, R., et al. 2012, MNRAS, 425, L66

Maiolino, R., Russell, H. R., Fabian, A. C., et al. 2017, Nature, 544, 202

Mazzucchelli, C., Bañados, E., Decarli, R., et al. 2017, ApJ, 834, 83

Mazzucchelli, C., Decarli, R., Farina, E. P., et al. 2019, ApJ, 881, 163

Meyer, R. A., Decarli, R., Walter, F., et al. 2022a, arXiv e-prints, arXiv:2201.09720

Meyer, R. A., Walter, F., Cicone, C., et al. 2022b, arXiv e-prints, arXiv:2201.08143

Mullaney, J. R., Alexander, D. M., Goulding, A. D., & Hickox, R. C. 2011, MNRAS, 414, 1082

Naab, T., Johansson, P. H., & Ostriker, J. P. 2009, ApJ, 699, L178

Neeleman, M., Bañados, E., Walter, F., et al. 2019, ApJ, 882, 10

Noeske, K. G., Weiner, B. J., Faber, S. M., et al. 2007, ApJ, 660, L43

Olsen, K., Greve, T. R., Narayanan, D., et al. 2017, ApJ, 846, 105

Omont, A., Petitjean, P., Guilloteau, S., et al. 1996, Nature, 382, 428

Oteo, I., Ivison, R. J., Dunne, L., et al. 2016, ApJ, 827, 34

Papovich, C., Dickinson, M., Giavalisco, M., Conselice, C. J., & Ferguson, H. C. 2005, ApJ, 631, 101

Patton, D. R., Wilson, K. D., Metrow, C. J., et al. 2020, MNRAS, 494, 4969

Pearson, W. J., Wang, L., Alpaslan, M., et al. 2019, A&A, 631, A51

Piconcelli, E., Vignali, C., Bianchi, S., et al. 2015, A&A, 574, L9

Planck Collaboration, Ade, P. A. R., Aghanim, N., et al. 2016, A&A, 594, A13

Popescu, C. C., Tuffs, R. J., Dopita, M. A., et al. 2011, A&A, 527, A109

Ramos Almeida, C. & Ricci, C. 2017, Nature Astronomy, 1, 679

Reines, A. E. & Volonteri, M. 2015, ApJ, 813, 82

Riechers, D. A., Bradford, C. M., Clements, D. L., et al. 2013, Nature, 496, 329

Riechers, D. A., Capak, P. L., Carilli, C. L., et al. 2010, ApJ, 720, L131

Riechers, D. A., Carilli, C. L., Capak, P. L., et al. 2014, ApJ, 796, 84

Riechers, D. A., Cooray, A., Pérez-Fournon, I., & Neri, R. 2021a, ApJ, 913, 141

Riechers, D. A., Hodge, J., Walter, F., Carilli, C. L., & Bertoldi, F. 2011, ApJ, 739, L31

Riechers, D. A., Nayyeri, H., Burgarella, D., et al. 2021b, ApJ, 907, 62

Rosenberg, M. J. F., van der Werf, P. P., Aalto, S., et al. 2015, ApJ, 801, 72

Sanders, D. B. & Mirabel, I. F. 1996, ARA&A, 34, 749

Sanders, D. B., Soifer, B. T., Elias, J. H., et al. 1988, ApJ, 325, 74

Scannapieco, C., White, S. D. M., Springel, V., & Tissera, P. B. 2011, MNRAS, 417, 154

Schawinski, K., Urry, C. M., Simmons, B. D., et al. 2014, MNRAS, 440, 889

Schmidt, M., Schneider, D. P., & Gunn, J. E. 1995, AJ, 110, 68

Scholtz, J., Alexander, D. M., Harrison, C. M., et al. 2018, MNRAS, 475, 1288

Scholtz, J., Harrison, C. M., Rosario, D. J., et al. 2020, MNRAS, 492, 3194

Scholtz, J., Harrison, C. M., Rosario, D. J., et al. 2021, MNRAS, 505, 5469

Scoville, N., Lee, N., Vanden Bout, P., et al. 2017, ApJ, 837, 150

Sijacki, D., Vogelsberger, M., Genel, S., et al. 2015, MNRAS, 452, 575

Silk, J. & Rees, M. J. 1998, A&A, 331, L1

Sparre, M. & Springel, V. 2016, MNRAS, 462, 2418

Spilker, J. S., Marrone, D. P., Aravena, M., et al. 2016, ApJ, 826, 112

Spilker, J. S., Phadke, K. A., Aravena, M., et al. 2020, ApJ, 905, 85

Springel, V., White, S. D. M., Jenkins, A., et al. 2005, Nature, 435, 629

Stacey, G. J., Geis, N., Genzel, R., et al. 1991, ApJ, 373, 423

Stacey, G. J., Hailey-Dunsheath, S., Ferkinhoff, C., et al. 2010, ApJ, 724, 957

Stanley, F., Harrison, C. M., Alexander, D. M., et al. 2018, MNRAS, 478, 3721

Stanley, F., Jolly, J. B., König, S., & Knudsen, K. K. 2019, A&A, 631, A78

Stanley, F., Knudsen, K. K., Aalto, S., et al. 2021, A&A, 646, A178

Stark, D. P. 2016, ARA&A, 54, 761

Steidel, C. C., Giavalisco, M., Pettini, M., Dickinson, M., & Adelberger, K. L. 1996, ApJ, 462, L17

Stern, D., Lansbury, G. B., Assef, R. J., et al. 2014, ApJ, 794, 102

Strickland, D. K. & Heckman, T. M. 2009, ApJ, 697, 2030

Sturm, E., González-Alfonso, E., Veilleux, S., et al. 2011, ApJ, 733, L16

Tacconi, L. J., Genzel, R., Saintonge, A., et al. 2018, ApJ, 853, 179

Tacconi, L. J., Genzel, R., Smail, I., et al. 2008, ApJ, 680, 246

Tadhunter, C. 2008, New A Rev., 52, 227

Thompson, A. R., Moran, J. M., & Swenson, George W., J. 2017, Interferometry and Synthesis in Radio Astronomy, 3rd Edition

Trakhtenbrot, B., Lira, P., Netzer, H., et al. 2017, ApJ, 836, 8

Tsai, C.-W., Eisenhardt, P. R. M., Wu, J., et al. 2015, ApJ, 805, 90

Urry, C. M. & Padovani, P. 1995, PASP, 107, 803

Vallini, L., Gallerani, S., Ferrara, A., Pallottini, A., & Yue, B. 2015, ApJ, 813, 36

van der Werf, P. P., Berciano Alba, A., Spaans, M., et al. 2011, ApJ, 741, L38

Veilleux, S., Maiolino, R., Bolatto, A. D., & Aalto, S. 2020, A&A Rev., 28, 2

Venemans, B. P., Walter, F., Neeleman, M., et al. 2020, ApJ, 904, 130

Vogelsberger, M., Genel, S., Springel, V., et al. 2014, Nature, 509, 177

Walter, F., Weiß, A., Downes, D., Decarli, R., & Henkel, C. 2011, ApJ, 730, 18

Wardlow, J. L., Simpson, J. M., Smail, I., et al. 2018, MNRAS, 479, 3879

Warren, S. J., Hewett, P. C., & Osmer, P. S. 1994, ApJ, 421, 412

Watson, D., Christensen, L., Knudsen, K. K., et al. 2015, Nature, 519, 327

Weiss, A., Downes, D., Walter, F., & Henkel, C. 2007, in Astronomical Society of the Pacific Conference Series, Vol. 375, From Z-Machines to ALMA: (Sub)Millimeter Spectroscopy of Galaxies, ed. A. J. Baker, J. Glenn, A. I. Harris, J. G. Mangum, & M. S. Yun, 25

Weiß, A., Henkel, C., Downes, D., & Walter, F. 2003, A&A, 409, L41

Willott, C. J., Percival, W. J., McLure, R. J., et al. 2005, ApJ, 626, 657

Wilson, T. L., Rohlfs, K., & Hüttemeister, S. 2013, Tools of Radio Astronomy

Wu, J., Bussmann, R. S., Tsai, C.-W., et al. 2014, ApJ, 793, 8

Wu, J., Tsai, C.-W., Sayers, J., et al. 2012, ApJ, 756, 96

Yan, H. & Lazarian, A. 2012, J. Quant. Spectr. Rad. Transf., 113, 1409

Yang, C., Omont, A., Beelen, A., et al. 2016, A&A, 595, A80

Yue, M., Fan, X., Schindler, J.-T., McGreer, I. D., & Huang, Y.-H. 2019, ApJ, 883, 141

Zhang, H. & Yan, H. 2018, MNRAS, 475, 2415

Zhang, H., Yan, H., & Dong, L. 2015, ApJ, 804, 142

Zhang, Z.-Y., Papadopoulos, P. P., Ivison, R. J., et al. 2016, Royal Society Open Science, 3, 160025